International Journal of Biological Macromolecules 321 (2025) 146636

Contents lists available at ScienceDirect

International Journal of Biological Macromolecules

journal homepage: www.elsevier.com/locate/ijbiomac

# Selective molecular probes for G-quadruplex and G-quadruplex–duplex junctions: Cyanine dye interactions and structural insight

Aleksey Vasilev [a,b], Diana Cheshmedzhieva [b], Hamzah Ahmed [c], Ona Raset [c], Gigliola Borgonovo [d], Stefania Mazzini [d], Roberto Artali [e], Marco Zuccolo [f], Raimundo Gargallo [c,*]

[a] Laboratory of Functional and Nanostructured Polymers, Institute of Polymers, Bulgarian Academy of Sciences, Akad. G. Bonchev Str., Bl. 103A, 1113 Sofia, Bulgaria
[b] Faculty of Chemistry and Pharmacy, Sofia University "St. Kliment Ohridski", 1 James Bourchier Blvd., 1164 Sofia, Bulgaria
[c] Department of Chemical Engineering and Analytical Chemistry, University of Barcelona, E-08028 Barcelona, Spain
[d] Department of Food, Environmental and Nutritional Sciences (DEFENS), University of Milan, 20133 Milan, Italy
[e] Scientia Advice di Roberto Artali, 20811 Cesano Maderno, MB, Italy
[f] Department of Agricultural and Environmental Sciences - Production, Landscape, Agroenergy (DiSAA), University of Milan, 20133 Milan, Italy

ARTICLE INFO

*Keywords:*
Cyanine dyes
Fluorescence
G-quadruplex
G-quadruplex/duplex junction
Hydrophilicity

ABSTRACT

There is growing interest in hybrid DNA structures, particularly G-quadruplex–duplex junctions, as potential ligand binding sites. In this work, we investigate the interaction of two cyanine dyes (R9 and 3b), which differ in hydrophilicity, with various DNA structures, including duplex DNA, parallel and antiparallel G-quadruplexes, and a G-quadruplex-duplex junction. We employed molecular spectroscopic techniques (UV–visible absorption, circular dichroism, fluorescence), nuclear magnetic resonance (NMR) spectroscopy, multivariate analysis, and molecular docking studies. UV–visible absorption and circular dichroism provided insights into dye aggregation and the overall interaction modes, while NMR and docking yielded structural details.

The results reveal that the two dyes exhibit distinct interactions with the studied DNA structures due to their differing behaviors in aqueous solution. The less polar 3b dye is aggregation-prone and prefers π-stacking with the terminal tetrads in the parallel G-quadruplex structure, leading to strong induced circular dichroism in the visible region and fluorescence responses toward parallel G-quadruplex. The more polar R9 dye forms defined non-stacking complexes, especially at structured duplex or G-quadruplex-duplex junction sites, showing selective fluorescence enhancement. NMR and molecular docking support the idea that R9 binds selectively and without aggregation, while 3b binds strongly and non-specifically, often resulting in precipitation.

## 1. Introduction

Apart from the well-known double helix, DNA may form other structures, such as G-quadruplex, i-motif, or triplex DNA, among others. These are frequently classified as non-canonical DNA structures. G-quadruplex (G4) structures are formed in DNA regions particularly rich in guanine bases. G4s have been the subject of research for many years due to the presence of guanine-rich DNA sequences at the ends of telomeres and near the promoter regions of some oncogenes. This triggered the study of their potential in vivo role because of their potential involvement in cellular physiological processes and diseases [1–4]. Nowadays, it is known that guanine-rich sequences within telomeres may fold into G4 structures, providing protection against nuclease degradation [2,5]. Additionally, the location of guanine-rich sequences in the promoter regions of cancer-related genes present an attractive target in gene regulation therapies [6–8].

The building block of G4s is the tetrad, a planar arrangement of four guanine bases held together by Hoogsteen bonds. Additionally, cations, such as $K^+$, $Na^+$ or $NH_4^+$, among others, can be placed inside a tetrad, or between two tetrads, depending on the ionic radius of the cation. A guanine-rich DNA strand of sufficient length may fold intramolecularly to form G4 structures in many ways, depending on the orientation of the guanine-rich domains. This results in different conformations, such as parallel, antiparallel or mixed G4 structures [9]. In addition, hybrid structures may be formed by a G4 and a duplex moiety, which is known as G4-duplex junction [10]. The interest in the study of the DNA

* Corresponding author.
*E-mail address:* raimon_gargallo@ub.edu (R. Gargallo).

https://doi.org/10.1016/j.ijbiomac.2025.146636
Received 17 June 2025; Received in revised form 18 July 2025; Accepted 5 August 2025
Available online 7 August 2025

sequences able to form these junctions has increased in the last years because these junctions may offer specific binding sites for some ligands, such as those used as biomolecular probes [11–13]. The stability of these highly ordered structures (for example, at elevated temperatures), may be increased by the binding of appropriate ligands [14]. Many specific ligands for G4 structures have been described. These ligands may interact with the G4 structures via several mechanisms, such as stacking on the terminal tetrads, intercalation between two tetrads, or groove binding [15,16].

In line with the above, we have recently described the synthesis of several cyanine dyes and the application of them as biomolecular probes for the fluorescent detection of single and double-stranded DNA and RNA [17,18]. This class of dyes is divided into several subgroups. The most widely used types of structures are monomethine cyanine dyes, which are widely used to label nucleic acids in PCR kits, flow cytometry and live-dead cell analysis. Additionally, polymethine cyanines are also applied as fluorogenic markers (so called "light-on markers") for binding proteins and nucleic acids. Asymmetric monomethine cyanine dyes exhibit little to no intrinsic fluorescence in solution due to the free rotation between their two heterocyclic rings. Upon binding to DNA, RNA, or proteins, the rotational freedom between the two heterocyclic rings is restricted. This induced structural rigidity inhibits non-radiative relaxation pathways and prevents the dissipation of absorbed light energy as heat, leading to a significant increase in fluorescence [19]. The introduction of substituents into each heterocycle leads to changes in the characteristics of the dye, as the nature and position of these substituents have a significant impact on their binding mode and affinity for polynucleotides, as well as on their spectroscopic properties and biological activity [20].

Another unique feature of all cyanine dyes is their ability to aggregate in solution or on specific surfaces, which significantly alters their photophysical properties. This phenomenon is called aggregachromism. In the case of cyanine dyes, aggregachromism is highly pronounced and leads to disappearance or, in some cases, appearance of absorption and fluorescence bands. The degree of aggregachromism may be strongly influenced by the polarity of the dye and its hydrophilic properties. As a result, the interaction with a given DNA structure may also be influenced. The G4 binding ability of a series trimethine cyanine dyes was reported by Nanjunda et al. [21]. In this work, the stabilizing effects of side chain and aromatic substituents on the interaction between Tel22 and symmetrical trimethyne cyanine dyes, derivatives of indolenine, were investigated. According to the studies, the strongest stabilizing effect is achieved by a combination of propyl trimethylammonium side substituents and halogen atoms bound to indolenine. Additionally, in the aforementioned work, the authors demonstrate the selectivity for different G4 architectures based on the formation of fluorescent aggregates of the studied dyes on oligonucleotide matrix [21]. The present work compares the influence of substituents bearing propionamide and propylpyridinium side groups, alongside a chlorine substituent in the quinoline core of the thiazole orange chromophore R9, and the influence of methyl substituents attached to the chromophore part of thiazole orange in dye 3b [18] [22] (Fig. 1).

The calculated dipole moments of the dyes are 23.41 and 5.95 D for R9 and 3b, respectively. R9 is a dicationic dye and exhibits limited permeability to cellular membranes [18]. This characteristic, common among similar fluorogenic dyes, may present a challenge for their application as probes for detecting RNA and DNA [23]. To overcome the limited membrane permeability of dicationic dye R9, a patented delivery technology, CellInject, was employed to enable efficient intracellular delivery of the dye. Upon successful entry, R9 demonstrates robust and detectable emission upon binding to RNA located in the cytoplasm and nuclei of the cells, confirming the intracellular release of the cationic dye from the CellInject carrier [18].

Both dyes were shown to strongly interact with some nucleic acid

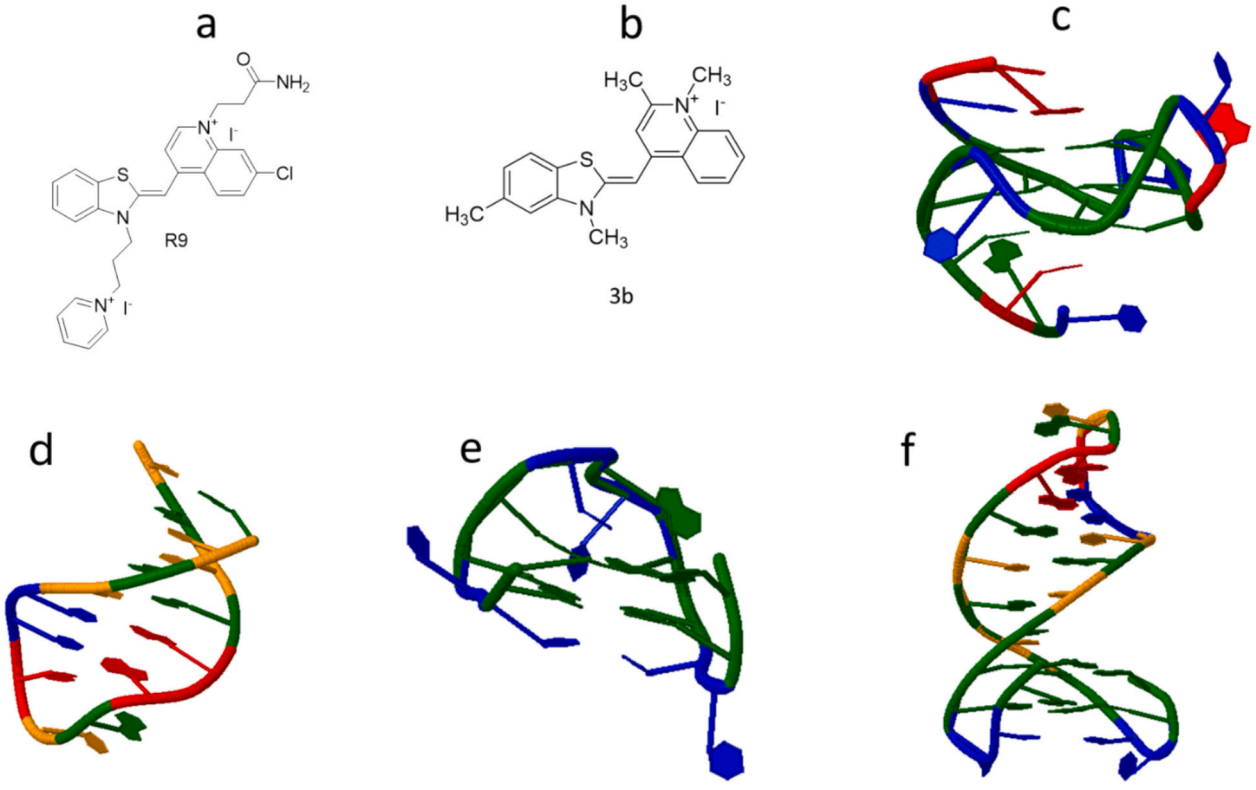


**Fig. 1.** Chemical structures of cyanine-based dyes and DNA structures studied in this work. (a) R9, (b) 3b, (c) Parallel G4 structure adopted by Pu22T14T23 (PDB code 1XAV, [24]), (d) hairpin DNA structure adopted by h28 (PDB code 2M8Y, [11]), (e) Antiparallel G4 adopted by TBA (PDB code 1QDF, [25]) (f) Antiparallel G4/DNA junction adopted by QDJ1 (PDB code 2M8Z, [11]). Green, orange, red and blue colors correspond to dG, dC, dA and dT nucleosides, respectively. (For interpretation of the references to color in this figure legend, the reader is referred to the web version of this article.)

structures, exhibiting a significant increase in fluorescence intensity with increasing nucleic acid concentration. However, they display different sensitivities: R9 demonstrates greater sensitivity toward RNA, while 3b shows enhanced affinity for double-stranded DNA (dsDNA). Fluorescence titration experiments revealed that upon contact with single or double-stranded DNA or RNA, the 3b dye exhibits aggregachromism on the surfaces of the respective structure [22]. Based on its fluorescent properties as well as its ability for aggrechromism, dye 3b has been proposed as suitable for use as a fluorogenic probe in biomolecular recognition techniques.

The main objective of this work is to study the interaction of the two cyanine dyes R9 and 3b with several DNA structures to assess the effects of hydrophobic and hydrophilic substituents on the spectroscopic properties of the resulting dye:DNA complexes for potential use in the detection of those structures. To do this, different spectroscopic techniques and experimental procedures will be used, together with multivariate data analysis and docking calculations.

The chosen DNA structures are shown in Fig. 1 and listed in Table 1. The T25 sequence has been considered as a control, as it cannot form any highly ordered structure, such as G4s or duplex DNA. It is expected, however, that in the considered medium (20 mM phosphate buffer and 50 mM KCl), T25 will exhibit a partial base stacking. The Pu22T14T23 DNA sequence folds intramolecularly to form a parallel G4-structure in a $K^+$-containing medium. This structure contains three tetrads and three propeller-type loops [24]. The sequence used contains two G-to-T mutations at the positions 14 and 23 in relation to the wild, original sequence found at the promoter region of the *c-myc* gene. The mutations were introduced in the wild sequence to reduce its large conformational variability, improving the resolution of NMR peaks, and its later assignment. The h28 sequence also folds intramolecularly and produces a hairpin stabilized by Watson-Crick base pairs, which may be used as a model for B-DNA structures [11]. The TBA (Thrombin Binding Aptamer) sequence folds intramolecularly into an antiparallel G4-structure, composed of two guanine tetrads, which are connected by two T-T loops and a T-G-T loop [25]. Finally, the QDJ1 sequence may form a hybrid structure containing an antiparallel G4 moiety, together with a duplex region [11]. The last-mentioned structure has been the subject of study due to the presence of a junction between both moieties that could favor a selective interaction with some ligands [10].

The results have shown distinct behaviors of the dyes in aqueous solutions, which influence their interactions with the DNA structures studied. The more charged dye (R9) exhibits a simpler binding mechanism, whereas the less charged and more hydrophobic dye (3b) tends to aggregate on the surface of parallel G4 structures. These differences correlate with their distinct fluorescence properties. For the G4–duplex junction, NMR analysis and molecular docking confirm that the interaction occurs specifically at the junction between the two structures.

**Table 1**
DNA sequences studied in this work.

| Name | Sequence (5′ to 3′) | Expected 3D structure at the experimental conditions | Reference |
|---|---|---|---|
| T25 | T25 | Unfolded strand | |
| Pu22T14T23 | TGA GGG TGG GTA GGG TGG GTA A | Parallel G4 | [24] |
| h28 | AGG AAG GAA AAG TTTT CTT TTC CTT CCT | Hairpin (or intramolecular) duplex | |
| TBA | GG TT GG TGT GG TT GG | Antiparallel G4 | [25] |
| QDJ1 | GGT TGG CGC GAA GCA TTC GCG GGT TGG | Antiparallel G4-duplex junction | [11] |

## 2. Experimental part

### 2.1. Reagents and solutions

The studied DNA sequences (Table 1) were purchased from Sigma-Aldrich (Merck KGaA, Germany) and were used without further purification. Each tube was dissolved to 100 micromolar by adding the appropriate volume of ultrapure water. The integrity of the DNA stock solutions was assessed by MALDI-TOF MS. Potassium phosphate (pH 7.4) buffer was also purchased from Merck KGaA, whereas KCl was purchased from PanReac AppliChem (Castellar del Vallès, Spain). Ultrapure MilliQ (Merck Millipore, MA, U.S.) water was used in all experiments.

The dyes 1-(3-amino-3-oxopropyl)-7-chloro-4-((3-(3-(pyridin-1-ium-1-yl)propyl)benzo[*d*]thiazol-2(3H)-ylidene)methyl)quinolin-1-ium iodide (R9) and (Z)-4-((3,5-dimethylbenzo[*d*]thiazol-2(3H)-ylidene) methyl)-1,2-dimethylquinolin-1-ium iodide (3b) were synthesized at the University of Sofia following procedures previously described [18,22]. A stock solution of both dyes was prepared by dissolving in DMSO at 1 mM concentration.

### 2.2. Instruments and apparatus

Absorbance spectra were recorded with an Agilent 8453 diode array spectrophotometer and Hellma quartz cells (10 mm path length, 400 and 1500 μl volume, Germany) were used.

CD spectra were recorded with a Jasco J-815 (MD, U.S.) spectropolarimeter equipped with a Peltier accessory for temperature control. In this case, Hellma quartz cells (10 mm path length, 3000 μl volume) were used. A 10 $L \cdot min^{-1}$ $N_2$ flow was used along the measurements. CD-monitored melting experiments were carried out in a stepwise fashion with at a 1 °C/min heating rate. Ellipticity values at chosen wavelengths were monitored along the heating curve. In addition, every 5 °C, the program acquired a complete CD spectrum. The CD spectra were smoothed by applying a Savitsky-Golay filter after subtraction of the blank.

A Bruker Avance 600 MHz spectrometer (Germany) available at the Unitech Cospect platform (University of Milan) was used to measure NMR spectra. A 5 mm triple-resonance probe with *z*-axis gradients and a variable temperature control unit was used.

An AB2 Aminco-Bowman (Thermo Fisher, MA, U.S.) spectrofluorimeter was used to record fluorescence spectra. For most of the measurements, voltage of the photomultiplier was set to 600 V, and excitation and emission slits were set to 4 nm. A Hellma quartz cell (2 × 10 mm path length, and 400 μl volume) was used. The temperature was set to 15 °C.

### 2.3. Experimental procedures

For the dependence of visible spectra of dyes with concentration, a 200 micromolar dye concentration was prepared in the medium (20 mM phosphate buffer, 50 mM KCl). Then, incremental volumes of this dye stock solution were added to 1 mL of medium. Molecular absorption spectra were measured from 350 to 600 nm at 20 °C. For the dependence of visible spectra of dyes with temperature, experiments were carried out by heating from 20 to 70 °C a dye solution. Molecular absorption spectra were measured from 350 to 600 nm spectra were measured every 2 °C, after an equilibration time of 3 min.

For the UV–visible study of the interaction of dyes with DNA structures, a 50 micromolar DNA stock solution was prepared in the medium (20 mM phosphate buffer, 50 mM KCl). Incremental volumes of this DNA stock solution were added to 400 μl of dye in the medium (1.5 micromolar dye, 20 mM phosphate buffer, 50 mM KCl). Molecular absorption spectra were measured from 350 to 600 nm at 20 °C. For the CD study of the interaction of dyes with DNA structures, a 400 micromolar dye stock solution was prepared in the medium (20 mM phosphate

buffer, 50 mM KCl). Incremental volumes of this dye stock solution were added to 1 mL of 2 micromolar DNA in the medium. CD spectra were measured from 235 to 550 nm at 20 °C. The CD spectrum of blank solution was removed from the CD spectra of DNA:dye mixtures. CD spectra were smoothed with a Savitsky-Golay filter as written in a Matlab® routine. Samples for CD-monitored melting experiments were prepared by mixing the appropriate reagents, heating at 85 °C for 10 min and cooling to room temperature overnight.

For NMR experiments, G4 oligonucleotides Pu22T14T23 and QDJ1 (70 OD), were dissolved in 0.55 mL $H_2O/D_2O$ 9:1 buffer solution having 70 mM KCl, 25 mM potassium phosphate and 50 mM KCl, 10 mM potassium phosphate respectively, pH = 7.0. NMR experiments were performed at 25 °C for Pu22T14T23 and 5 °C for QDJ1. Pu22T14T23 and QDJ1 signals were attributed following the previous assignments [11,26]. Water suppression was achieved by excitation sculpting sequence from standard Bruker library. The oligonucleotides were heated at 95 °C for 3 min and then cooled overnight at room temperature. For interaction studies with both dyes stock solutions were prepared in DMSO-$d_6$ at a concentration of 13.2 mM for R9 and 43 mM for 3b. $^1$H NMR titrations for R9 were performed by adding increasing amounts of the dye to the oligonucleotide solution until R = [dye]:[Pu22T14T23] = 2.0 and [dye]:[QDJ1] = 2.0 was reached, while for 3b until R = [dye]:[Pu22T14T23] = 10.0 and [dye]:[QDJ1] = 1.0 was reached. The concentration of the DMSO in the sample solution was below 10 % to avoid affecting the G4 conformation. Phase sensitive NOESY spectra of the complex of QDJ1 with both dyes and of Pu22T14T23 with both dyes were acquired at 5 °C and 25 °C respectively, in TPPI mode, with 2048 × 1024 complex FIDs, with $t_{mix}$ ranging from 300 and 150 ms. The spectra were transformed and weighed with a 90° shifted sine-bell squared function to 4 K × 4 K real data points. TOCSY spectra were acquired with 80 ms of mixing time.

For fluorescence measurements, samples consisted of mixtures of dye (0.7 micromolar) and DNA (2.1 micromolar) in 20 mM phosphate buffer and 50 mM KCl. Excitation-emission maps (EEMs) were measured at 15 °C. For 3b, excitation range was 400 to 600 nm, and emission range was 500 to 700 nm.

### 2.4. Docking studies

Both dyes were prepared for docking by adding hydrogen atoms and assigning charges, followed by energy minimization of the resulting 3D structures. Structural models of QDJ1 (PDB ID: 2M8Z) and Pu22T14T23 (PDB ID: 1AXV) were retrieved from the RCSB Protein Data Bank [11,24]. The interactions between the two 3b dyes and the QDJ1 and Pu22T14T23 models were evaluated using YASARA Structure software [27], which utilizes the AutoDock Vina [28] molecular docking algorithm. Docking simulations were performed with the dock_run.mcr macro in YASARA Structure, using 100 docking iterations, specifying 10 binding modes, a search exhaustiveness of 8, and a maximum allowed energy difference of 3 kcal/mol. Each docking result was ranked according to the lowest binding free energy (kcal/mol). The most favorable complexes were selected based on binding energy and agreement with experimental findings. These optimal conformations were further refined using the steepest descent conjugate gradient method, applying the OL15 modification of the Amber force field as implemented in YASARA Structure [29]. The final YOB files were converted into PDB format and analyzed for dye positioning and base contacts using three-dimensional visualization in BIOVIA Discovery Studio (DS) visualizer [30].

### 2.5. Analysis of data recorded along CD-monitored melting experiments

Ellipticity values recorded at a single wavelength during CD-monitored melting experiments were analyzed using the van't Hoff equation:

$$lnK_{folding} = -\frac{\Delta H^o}{RT} + \frac{\Delta S^o}{R} \quad (1)$$

where $\Delta H^o$ and $\Delta S^o$ represent the standard enthalpy and entropy changes associated with the folding process, respectively, and they are assumed to be constant over the studied temperature range. The equilibrium constant for folding ($K_{folding}$) at each temperature was determined from the experimental CD traces by modeling the process as a two-step folding transition [31,32].

### 2.6. Multivariate data analysis

Multivariate analysis based on the Multivariate Curve Resolution-Alternating Least Squares method (MCR-ALS) was applied to resolve DNA species in some titrations [33,34]. This analysis utilized the measured spectra as a function of DNA:dye ratio from 350 to 600 nm. By using these spectra as matrix **D** with *m* ratios x *n* wavelength values, it is possible to resolve or deconvolute the information into the concentration and spectral profiles of the pure components or species present. MCR-ALS has been applied to a wide range of problems, including the investigation of chemical and conformational equilibria of nucleic acids using spectroscopic techniques [34–36]. A complete description of the MCR-ALS data analysis and its practical implementation using the recommended freeware, MCR-ALS GUI 2.0 graphical interface, which operates within the MATLAB environment, can be found at the address https://mcrals.wordpress.com/.

## 3. Results

### 3.1. Study of dye aggregation

First, the dependence of the visible absorbance spectra of both dyes with concentration and temperature was studied to gain knowledge about the potential formation of aggregates at the experimental conditions (20 mM phosphate buffer, 50 mM KCl, 15–20 °C). It is expected that an increase in dye concentration will promote the formation of aggregates, whereas an increase in temperature will promote the transition to the monomer forms.

Fig. 2a shows the visible spectra of dye R9, which is the most charged dye, as a function of dye concentration between 2 and 15 micromolar, approximately. A 2 micromolar solution showed a strong absorption band at 505 nm accompanied by a shoulder around 480 nm. Minor changes were observed when concentration increased. To evaluate the potential bathochromic and hypsochromic shifts produced by the increased concentration in more detail, the normalized spectra to equal length at 2 and 15 micromolar concentration are also given (Fig. 2c, blue and yellow lines). As a result, the focus is on the hypsochromic or bathochromic shifts, rather than on the hyperchromicity or hypochromicity produced along the experiment [37]. Upon increasing dye concentration, no clear spectral changes were observed (Fig. 2c). Therefore, it was deduced that by increasing concentration within the studied range, no aggregation was produced. Fig. 2b shows the dependence of the visible spectra of dye R9 with temperature. This experiment has been carried out using the sample at the highest dye concentration (15 micromolar) prepared in the previous experiment (Fig. 2a). For dye R9, increasing the temperature did not produce any spectral change (Fig. 2c, red line), in coherence with the lack of aggregation observed in Fig. 2a.

Similar experiments were conducted with 3b, the less charged dye. A 2 μM solution at 20 °C exhibited absorption bands centered at 470 and 500 nm (Fig. 2d). Upon increasing the dye concentration, the band at 470 nm displayed a stronger hyperchromic effect than the band at 500 nm. The change in spectral shape due to concentration variations is also evident when examining the normalized intensities of both bands (Fig. 2f, blue and yellow lines). Conversely, increasing the temperature

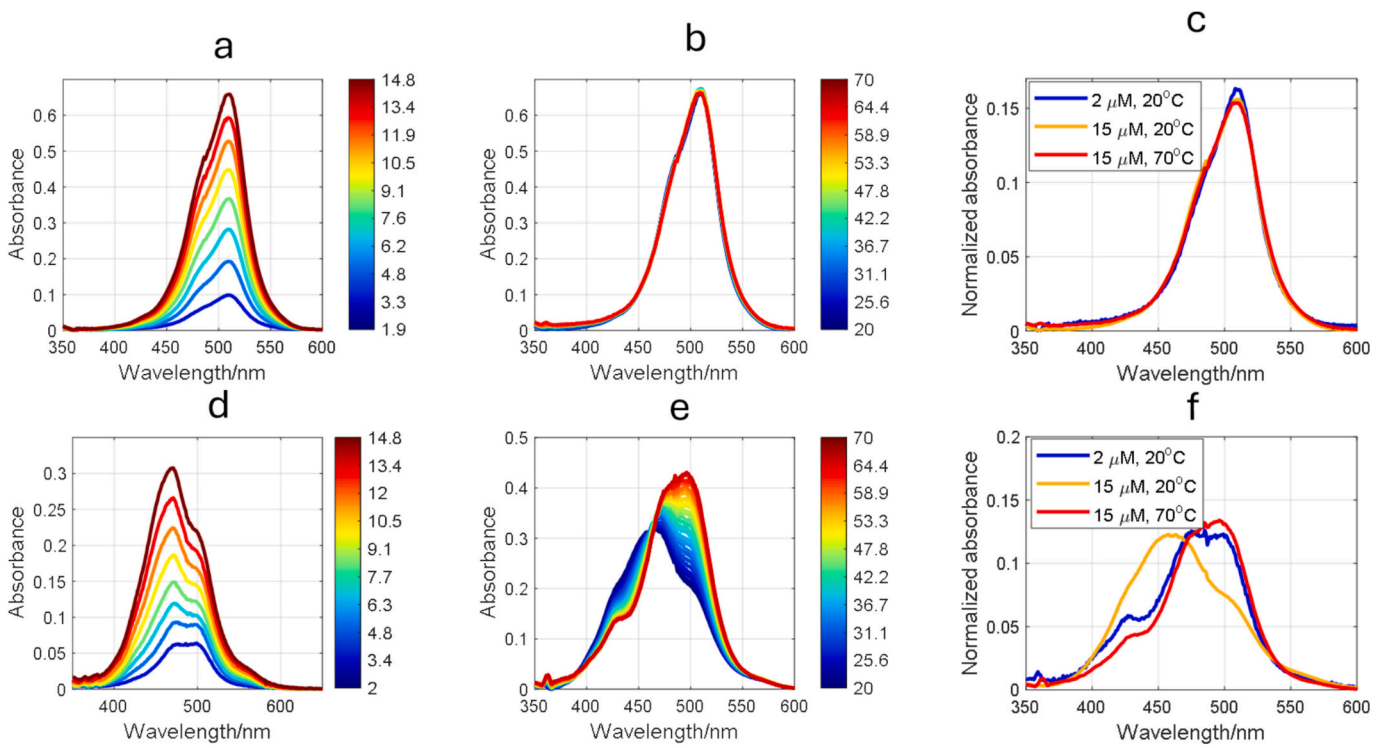


**Fig. 2.** Dependence of visible spectra of dyes with concentration (a, d), with temperature (b, e) and normalized spectra (c, f). Data for dye R9 (a-c), and 3b (d-f). Dye concentration (in micromolar) in (a) and (d) are given as color bars. Temperature values in (b) and (e) are given as color bars. Experimental conditions were 20 mM phosphate buffer, pH 7.4, 50 mM KCl.

of the 15 μM solution from 20 °C to 70 °C led to a significant increase in intensity at 500 nm (Fig. 2e). Consequently, the normalized spectra of the 2 μM solution at 20 °C and the 15 μM solution at 70 °C show good agreement (Fig. 2f, blue and red lines, respectively). In summary, these observations suggest that the band at 500 nm corresponds to the monomer form, whereas the band at 470 nm is associated with H-aggregates [38].

### 3.2. *Theoretical calculations on the formation of dye aggregates*

As shown in Fig. 2, monomethine cyanine dyes may aggregate in aqueous solutions due to their hydrophobic nature. The ratio of absorption maxima for dimer and monomer species indicates that dye 3b exhibits a stronger tendency to aggregate, as its spectrum is dominated by the absorption band corresponding to dimers. In contrast, for R9, the band at 480 nm, which is associated with the dimer, appears only as a shoulder, indicating a weaker degree of aggregation. The hydrophobic nature and polarizability of the dyes are thought to promote π-stacking interactions, leading to the formation of dimers and larger aggregates. To better understand these interactions, the structures of potential dimers have been examined theoretically. According to the literature, two general types of dimers are commonly observed: H- and J-dimers

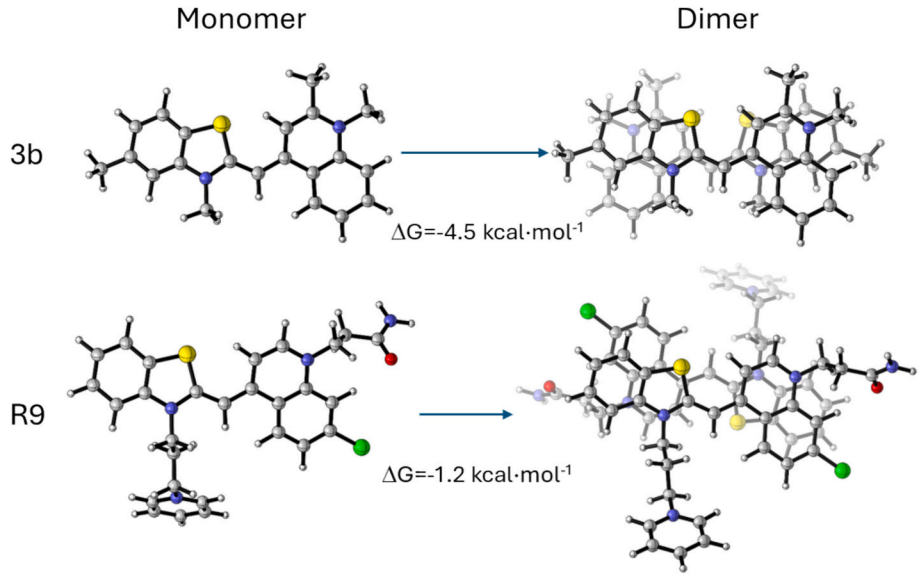


**Fig. 3.** M062X/6-31G(d,p) optimized molecular structures of the monomer and the most stable H- - dimers of 3b and R9 in water medium.

[39–41]. The geometry and the relative energies of various dimers of 3b were investigated theoretically and detailed results are provided in Table S1. H-dimers are formed when two dye molecules stack directly on top of each other (Fig. S1A), while J-dimers are characterized by a slipped, head-to-tail arrangement of the molecules (Fig. S1B). Among the structures examined, H-dimers of 3b are generally more stable than J-dimers. The most stable H-dimer of 3b is given at Fig. 3. These theoretical findings are consistent with experimental observations, particularly the concentration- and temperature-dependent changes in the visible absorbance spectra of both dyes discussed earlier.

The Gibbs free energy change of dimer formation (ΔG) was modeled employing the following reaction $2D \rightarrow (D)_2$ and it shows the energy difference between the separated molecules and the dimer. The negative ΔG values mean that the dimer formation is spontaneous and implies that dimers are energetically more favorable than monomeric dyes. The geometry of both the monomer dyes and their corresponding dimers were optimized at M062X/6-31G(d,p) level of theory using Gaussian 16 software package [42]. The computed value for Gibbs free energy of dimer formation for the H2 dimer of dye 3b is −4.5 kcal/mol, whereas for dye R9 is −1.2 kcal/mol. These Gibbs free energy (ΔG) values, along with the previously discussed molecular absorption spectra, indicate that 3b dye is more prone to aggregation compared to R9.

### 3.3. Study of the interaction of dyes with DNA structures by molecular absorption spectroscopy

After studying the ability of the considered dyes to form aggregates, their interactions with different DNA sequences capable of forming duplex and quadruplex structures were investigated.

First, spectroscopically-monitored titrations were carried out using dye R9, which exhibits a maximum absorption at 505 nm, in the presence of various DNA sequences (Fig. 4a–e). In all cases, the absorption band of the dye underwent a red shift, accompanied by either hyperchromic or hypochromic effects. The addition of a partially folded DNA strand (T25) at a DNA:dye ratio of approximately 2:1 resulted in small hypochromic and bathochromic shifts (+4 nm) (Fig. 4a). Since this DNA sequence lacks a highly organized structure, these spectral changes were attributed to electrostatic, non-specific interactions between the dye and T25 at low DNA:dye ratios.

When more structured DNA sequences were introduced, such as the parallel G4 adopted by Pu22T14T23, additional spectral changes were observed beyond those seen with T25, including a slight hyperchromic effect at high DNA:dye ratios (Fig. 4b). Under experimental conditions, the absorbance maximum shifted to 518 nm (+13 nm). Similar behavior was observed for h28 (+9 nm, Fig. 4c) and QDJ1 (+12 nm, Fig. 4e). In contrast, the addition of the antiparallel G4 adopted by TBA induced spectral changes like those observed with T25 (+5 nm, Fig. 4d). Since the drop in absorbance at low DNA:R9 ratios was comparable across all cases and resembled that observed for T25, it was concluded that electrostatic interactions were present in all instances at low DNA:dye ratios. At higher DNA concentrations, the magnitude of the observed hyperchromic shifts pointed to other mechanisms, such as groove binding, end-stacking or intercalation.

For 3b, interaction with the partially folded T25 sequence resulted in a pronounced hypochromic effect accompanied by a slight bathochromic shift (Fig. 4f). Like dye R9 (Fig. 4a), these observations were attributed to electrostatic interactions. A more complex behavior was inferred from the spectral changes observed during the titration of 3b with other DNA structures (Fig. 4g–j). The addition of Pu22T14T23 initially caused a drop in absorbance, likely due to electrostatic interactions, followed by a significant increase in absorbance at 481 and 510 nm, suggesting a distinct mode of interaction. A comparable trend was observed in the interaction between the h28 hairpin and dye 3b. However, the relative intensities of the absorption bands at the end of the titration (Fig. 4h) differed from those seen with Pu22T14T23 (Fig. 4g). As described above, the band at 500 nm corresponds to the monomer form, whereas the band at 470 nm is associated with H-aggregates. Interestingly, the interaction of dye 3b with the QDJ1 G4-duplex junction (Fig. 4j) and with the duplex h28 seems to involve the monomer form. On the other hand, the interaction of the dye with the parallel Pu22T14T23 seems to be mostly due to the H-aggregates. Finally, the interaction of dye 3b with TBA was similar to that observed with T25, except for the species present at a 1:1 DNA:dye ratio.

To get more quantitative information about the spectral changes occurring along the titration of dyes R9 and 3b with DNA structures, the MCR-ALS method was applied to analyze the set of spectra measured along it. The method allows the calculation of the concentration profiles and pure spectra for the number of species or components considered in the deconvolution of the experimental spectra. However, assessing the correct number of species is not straightforward. For the spectra shown in Fig. 4, the analysis was carried out considering either two, three or four species. When only two components were considered, the data recorded during the titrations of dye R9 with the five sequences was well fitted (Fig. S2). In all these cases, the lack of fit (i.e., the experimental data not explained by the model of concentration and pure spectra) of the model considering two components was around 1.5 %. The explanation of the two components is as follows: the first component, which was present at the beginning of the titration, was related to dye R9,

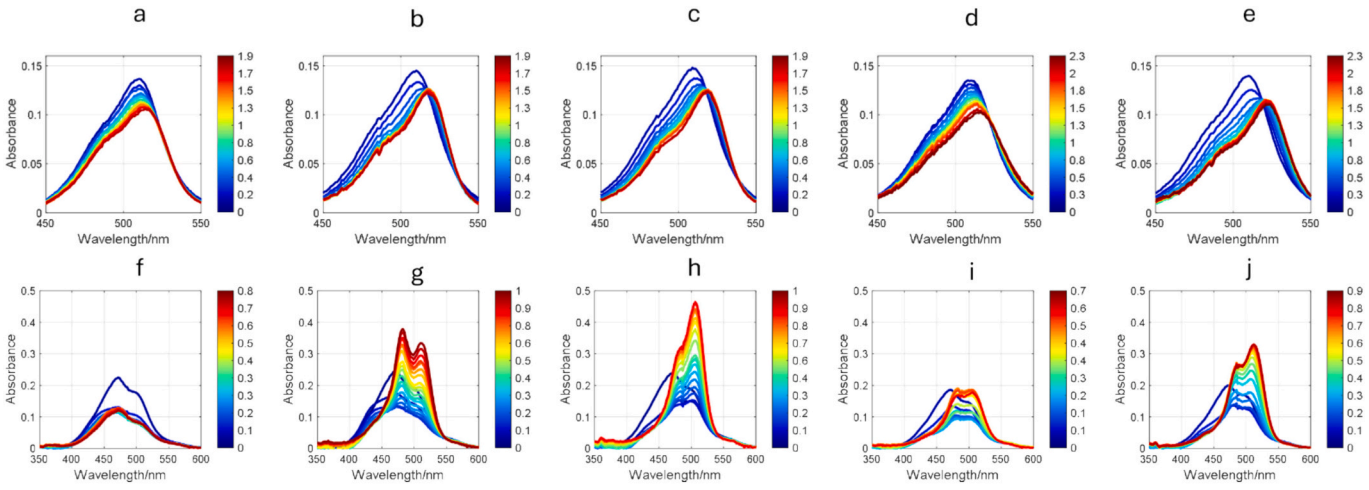


**Fig. 4.** Effect of addition of DNA sequences to R9 (a-e) and 3b (f-j). DNA sequences were T25 (a, f), Pu22T14T23 (b, g), h28 (c, h), TBA (d, i), and QDJ1 (e, j). Experimental conditions were 20 mM phosphate buffer, pH 7.4, 50 mM KCl, 20 °C. Color bars indicate the DNA:dye ratio. The initial R9 and 3b dye concentrations were 4 and 9 micromolar, respectively.

whereas the second component, which was the major species at the end of the titration, was related to the DNA:dye complex. Hence, it was deduced that only one interaction complex was detected. For T25 and TBA, the concentration profiles showed a smaller cooperative process than in the case of Pu22T14T23, h28 or QDJ1 structures.

Regarding the titrations of 3b dye with Pu22T14T23, h28, TBA or QDJ1, the lack of fit of the model considering three species was around 7.5 % in comparison to that obtained with a model of four species (around 2 %). Therefore, four components were deemed necessary to satisfactorily deconvolute the data set in these cases (Fig. S3). On the other hand, data measured during the titration of dye 3b with T25 were well explained with a simpler model of three species. The species the concentration and pure spectra of which are colored in blue refers to the free, uncomplexed dye. The "red" species, which is present at low DNA: dye ratios, would be related to the aggregation of the ligand on DNA surface, as its pure spectrum resembles that observed at high dye concentration (Fig. 2f). The "yellow" and "purple" species would be related to DNA:dye complexes with smaller aggregation ratio, as the position of the absorbance bands resemble more that of the monomer form of dye (Fig. 2f). In summary, it was clear that the mode of interaction of dye 3b with the considered structures was much more complex, even involving more than one interaction complex, than that of the more polar dye R9.

### 3.4. Study of the interaction of dyes with DNA structures by circular dichroism spectroscopy

Circular dichroism (CD) spectroscopy has been used to gain insight into the binding mechanism of dyes to the considered DNA structures [43]. Both dyes are achiral and do not exhibit an intrinsic CD spectrum. Similarly, DNA itself does not absorb in the visible region, meaning no CD signal is observed in this region for isolated DNA. However, the interaction of DNA with an achiral molecule can induce an ICD (induced CD) signal in the visible region. The appearance and shape of this ICD signal may provide clues about the dye's mode of interaction with DNA, such as intercalation, end-stacking, or aggregation [16]. Additionally, potential spectral changes in the UV region of the DNA CD spectrum upon dye addition may indicate conformational variations caused by the interaction.

Fig. 5 presents the CD spectra of the structures studied in the absence and presence of both dyes. For Pu22T14T23, the addition of either ligand did not induce any significant conformational change, as indicated by the preservation of the CD spectrum in the UV region, where DNA absorbs (Fig. 5a). However, the two dyes exhibit distinct ICD signals. The addition of dye 3b resulted in a well-defined bisignate exciton signal centered at 500 nm. The positions of the positive and negative signals closely resemble those observed for parallel DNA structures, suggesting a head-to-tail aggregation of dye molecules on the G4 surface [44,45]. In contrast, the presence of R9 generated only a minimal ICD signal at the tested dye and DNA concentrations.

As observed with Pu22T14T23, the addition of both dyes to the hairpin structure formed by the h28 sequence did not induce any significant conformational changes (Fig. 5b). However, the addition of the R9 molecule led to the appearance of a negative ICD signal at 525 nm, which became more pronounced when the dye-to-DNA ratio was increased to 10:1 (not shown). This negative ICD signal has been associated with an intercalative binding mechanism [16,46]. For the antiparallel G4 structure adopted by TBA (Fig. 5c), the addition of R9 and 3b caused slight conformational changes, as indicated by minor variations in ellipticity within the UV region. However, the most pronounced effect was observed with dye 3b, which generated a strong bisignate signal centered at 500 nm, which suggests a head-to-tail aggregation of dye molecules on the G4 structure. Finally, both dyes produced clear conformational changes on the hybrid structure adopted by QDJ1, as deduced from the spectral variations in the UV region (Fig. 5d). However, only a weak negative ICD was clearly observed at 525 nm in presence of dye 3b.

### 3.5. Melting experiments

To gain further understanding of the interaction between both dyes and DNA structures, CD-monitored melting experiments were carried out (Fig. 6). From the corresponding ellipticity traces, thermodynamic analysis has been done (Table 2).

As expected for a parallel G4 structure containing three tetrads, the

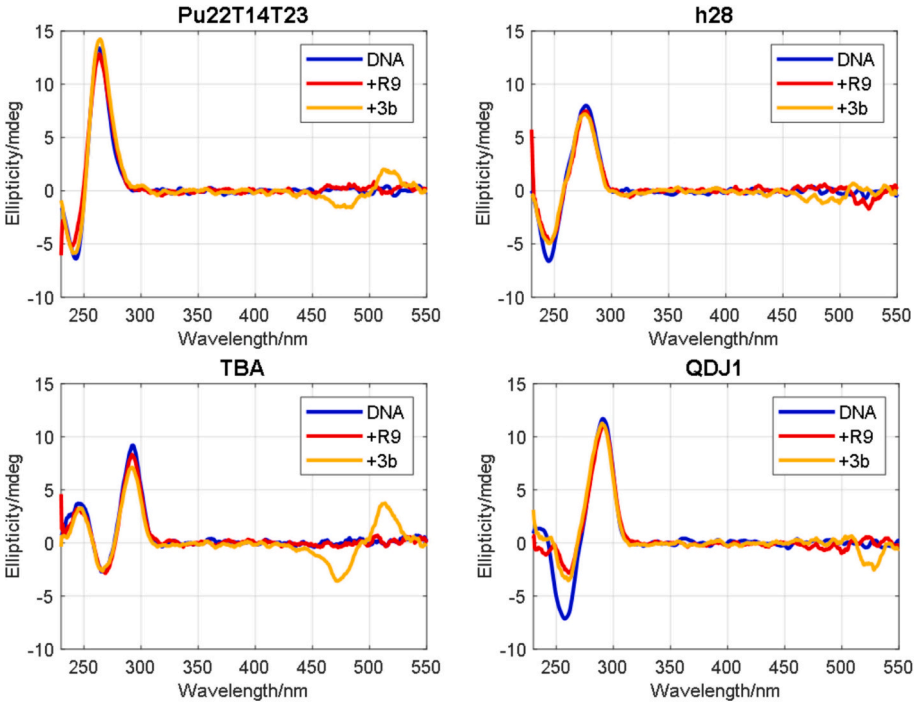


**Fig. 5.** CD spectra of mixtures of DNAs and dyes. (a) Pu22T14T23, (b) h28, (c) TBA, (d) QDJ1. DNA and dye concentrations were 2 and 6 micromolar, respectively. Experimental conditions were 20 mM phosphate buffer, pH 7.4, 50 mM KCl, 20 °C.

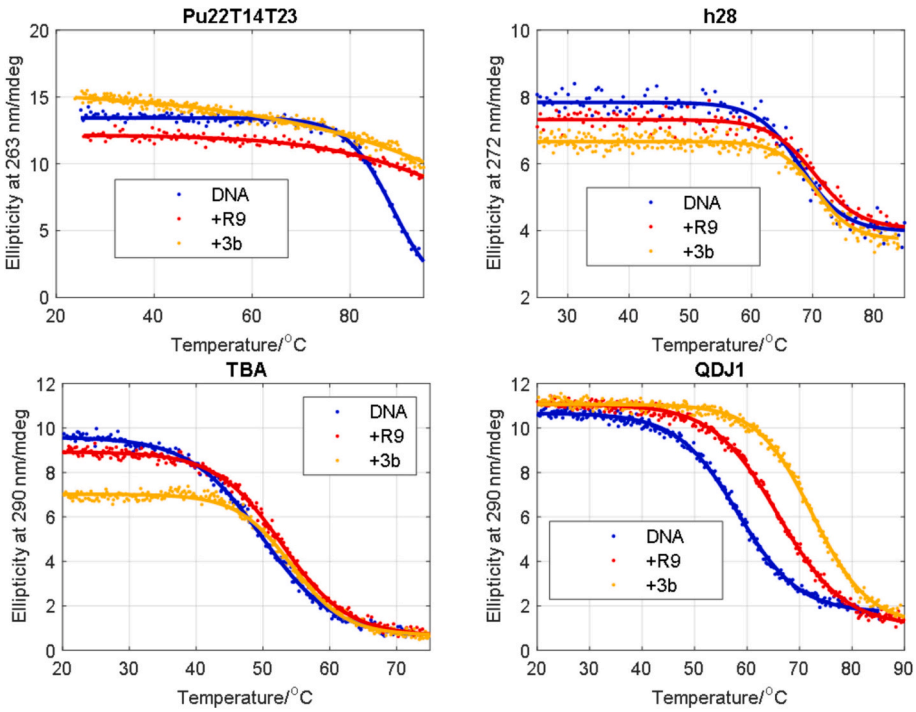


**Fig. 6.** CD-monitored melting experiments of DNA:dye mixtures. DNA and dye concentration were 2 and 6 micromolar, respectively. Experiments carried out at 20 mM phosphate buffer and 50 mM KCl.

**Table 2**
Thermodynamic analysis of CD-monitored melting experiments. For this analysis, a two-step folding process has been considered, as well as constant values of heat capacities through the studied temperature range. The changes in enthalpy and free Gibbs energy are given in kcal·mol$^{-1}$, whereas the changes in entropy are given in cal·K$^{-1}$·mol$^{-1}$. These values are accompanied by estimates of the associated incertitude, which have not been included in the table.

| | Without ligand [1] | | | | R9 (more charged) [1] | | | | 3b (less charged) [1] | | | |
|---|---|---|---|---|---|---|---|---|---|---|---|---|
| | $T_m$ (°C) | $\Delta H^o$ | $\Delta S^o$ | $\Delta G^o_{37}$ | $T_m$ (°C) | $\Delta H^o$ | $\Delta S^o$ | $\Delta G^o_{37}$ | $T_m$ (°C) | $\Delta H^o$ | $\Delta S^o$ | $\Delta G^o_{37}$ |
| Pu22T14T23 | 88.6 ± 0.8 | −55.7 | −153.9 | −7.9 | > 95 | – | – | – | > 95 | – | – | – |
| H28 | 68.0 ± 0.5 | −65.1 | −190.7 | −5.9 | 70.3 ± 0.6 | −64.4 | −187.4 | −6.2 | 70.5 ± 0.4 | −78.2 | −227.6 | −7.6 |
| TBA | 49.9 ± 0.2 | −38.4 | −118.9 | −1.5 | 52.8 ± 0.2 | −43.0 | −131.9 | −2.1 | 54.2 ± 0.2 | −52.4 | −160.1 | −2.7 |
| QDJ1 | 58.2 ± 0.2 | −32.3 | −97 | −2.1 | 65.3 ± 0.7 | −31.1 | −91.8 | −2.5 | 72.5 ± 0.3 | −44.8 | −129.5 | −4.6 |

stability of Pu22T14T23 is remarkably high ($T_m$ equal to 88.6 ± 0.8 °C). Therefore, it is not possible to know which ligand stabilizes the structure more because, in both cases, the unfolding of the structure does not reach 50 % at 95 °C (Fig. 6a). It is therefore not possible to determine with acceptable accuracy the value of the $T_m$ and the thermodynamic parameters associated with unfolding.

The hairpin formed by h28 sequence folds with a $T_m$ value equal to 68.0 ± 0.5 °C. Both dyes stabilize the hairpin to a similar degree, increasing the $T_m$ by 2 °C in both cases. However, the 3b ligand stabilizes ΔG value slightly more at 37 °C.

As expected for a G4 that only contains two tetrads, TBA forms a structure that is less stable in response to temperature changes than that formed by Pu22T14T23. Accordingly, TBA both shows lower $T_m$ values and a smaller change in free Gibbs energy. As is the case for h28, a slightly higher stabilization of 3b over R9 is observed for TBA.

Finally, QDJ1 forms a G4-duplex junction structure (Fig. 1f). At the monitored wavelength, unfolding of this structure occurs in a two-step process, i.e., both moieties unfold simultaneously with a $T_m$ value equal to 58.2 ± 0.2 °C. As the antiparallel G4 part of QDJ1 is composed of two tetrads, such as the G4 antiparallel formed by TBA, the higher $T_m$ value of QDJ1 in relation to that of TBA (49.9 ± 0.2 °C) should be related to the stabilization provided by the additional duplex moiety. For QDJ1, the presence of 3b dye clearly increases the stability of the structure, both in terms of $T_m$ and ΔG at 37 °C.

### *3.6. Study of the interaction of dyes with DNA structures by NMR spectroscopy*

To investigate the binding mode of both dyes with Pu22T14T23 and QDJ1 at the atomic level, NMR spectroscopy was employed. The presence of well-resolved and sharp signals in the δ 10.00–12.00 ppm range in the $^1$H NMR spectra support the formation of a single, well-defined G4 structure, consisting of three G-quartets in Pu22T14T23 and two in QDJ1. Additionally, in the case of QDJ1, distinct signals between δ 12.25 and 14.00 ppm indicate the formation of Watson-Crick hydrogen bonds, consistent with a characteristic hairpin loop. Titration experiments with increasing concentrations of both dyes were conducted, and variations in chemical shifts along with broadening of the imino proton signals were monitored. The $^1$H NMR spectra of the Pu22T14T23 and QDJ1 complexes with both dyes are presented in Figs. 7–10.

#### *3.6.1. Complexes of Pu22T14T23 with dyes 3b and R9*

The addition of dye 3b to Pu22T14T23 had a notable effect on the imino peaks (Fig. 7a). The spectra at R = [3b]:[Pu22T14T23] ratio till to 1.0 exhibit substantially only a peak broadening. Continuing the titration experiment with an excess of 3b, we observed an initial severe broadening ($R$ = 2.0 and 4.0) indicating a non-specific binding to the parallel G4. This suggests an intermediate exchange regime between free G4 and the complex. Nevertheless, increasing the R ratio up to

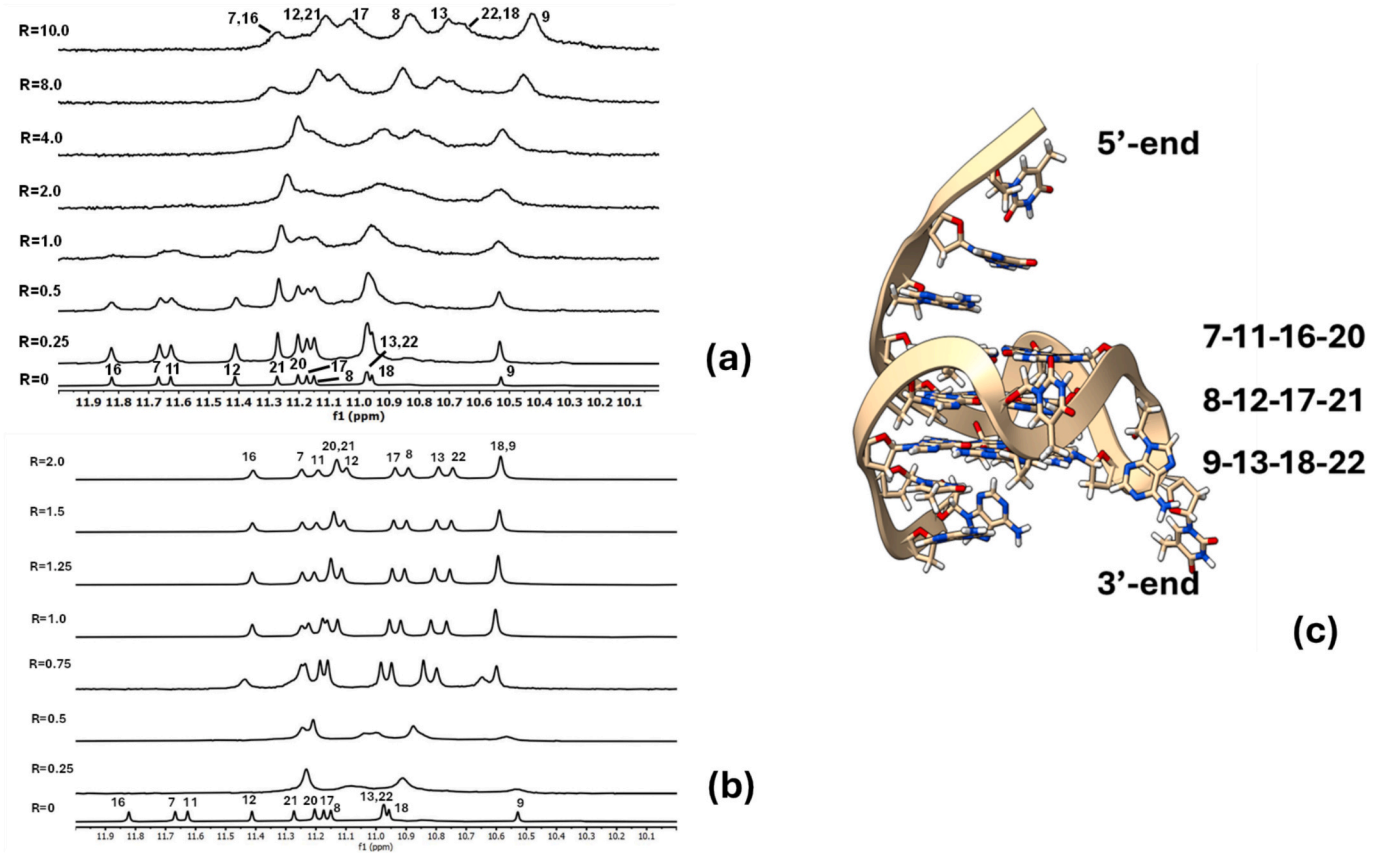


**Fig. 7.** Imino proton region of the 1D NMR titration spectra of Pu22T14T23 (a) with 3b at 25 °C in $H_2O/D_2O$ (9:1), 25 mM $KH_2PO_4$, 70 mM KCl, pH 6.9 and (b) with R9 at 25 °C in $H_2O/D_2O$ (9:1), 25 mM $KH_2PO_4$, 70 mM KCl, pH 7.0, at different R = [ligands]:[DNA] ratios; (c) a schematic representation of Pu22T14T23 showing the numbering of guanine bases involved in the formation of tetrads.

10.00, the signals became slightly sharper and showed an up-field shift in accordance with the interactions at the 3′ and 5′-end binding sites as proved by NOESY 2D experiment (Fig. S4 and Table S2). Unfortunately, no NOEs interactions were detected because of the overly broad signals.

Changes in the resonances of the imino protons were observed also in the titration experiment with R9 (Fig. 7b). These resonances at low R ratio ($R = 0.25$ and 0.5) became broad. Then, as the titration progressed, these peaks gradually became sharp and shifted, clearly indicating the formation of a well-defined DNA 1:2 non-covalent complex. The largest shifts were observed for the signals G7, G11, G16 and G18 representing the imino protons bound to the 3′-end and 5′-end external G-tetrads (Fig. 7c), whereas the signals corresponding to the protons in the middle tetrad exhibited minimal shift (Table S3).

The assignment of the guanine imino resonances was conducted by following the up-field G9-NH signal at 10.58 ppm. G8-NH and G7-NH were assigned through their sequential NOEs. The overlapped signal at 10.58 ppm was attributed to G18-NH basing on the NOE between G18-NH and G13-NH, like the NOE between G9-NH and G22-NH. The sequence G11-NH, G12-NH and G13-NH was assigned by their sequential interactions. As a result, G17-NH and G16-NH were assigned, confirming the assignment of G18-NH. The relatively constant G20-NH overlapped with G21-NH conforming the assignment of G22-NH (see Fig. 8a).

The assignments of the aromatic protons for the guanines were made by observing inter-residue NOE interactions with the imino NH protons, which reproduce the complete patterns of the inner and 3′-end tetrads, and a partial pattern for the 5′-end tetrad (Fig. 8b). Additionally, in the aromatic region, protons attributed to the R9 ligand can be observed (Fig. 8c). A detailed analysis of the NOESY spectrum of the Pu22T14T23: R9 complex (Fig. 8b) led to the conclusion that one ligand molecule interacts with the 5′-end tetrad, while the other binds to the 3′-end tetrad, as indicated by key intermolecular NOE contacts. In particular, NH9 and NH18 showed NOE interactions with H2c and H6c protons of the pyridinium ring C (Fig. 8d). NH13 and NH18 exhibited distinct NOEs with aromatic protons of ring system B. Additionally, NOE interaction between NH13 and the proton of the olefinic bridge was detected. Eventually, NH7 and NH11 showed NOEs with aromatic protons of ring system A.

### 3.6.2. *Complexes of QDJ1 and dyes 3b and R9*

Titration of QDJ1 with dye 3b led to the appearance of a new set of signals even at sub-stoichiometric dye concentrations (Fig. 9a), indicative of a slow exchange regime between the free and bound states of the G4 and dye. These signals were clearly detectable in the imino proton region, whereas signal assignment in the aromatic region was hindered by spectral overlap. Specifically, additional Hoogsteen G imino resonances emerged concurrently with the complete disappearance of certain signals from the free oligonucleotide upon reaching a $R = 1.0$ (Fig. 9a). In contrast, the downfield-shifted Watson-Crick imino signals displayed only slight line broadening, suggesting limited perturbation of the duplex domain.

Based on previously assigned resonances for the free QDJ1 [11], analysis of the NOESY spectrum revealed both inter-residue and exchange cross-peaks between the free and bound forms, allowing identification of several imino resonances in the QDJ1:3b complex (Fig. 9b and Table S4). Perturbations induced by the ligand primarily affected residues near G8 and at the G4–duplex junction (G21 and G22), supporting a preferential binding mode localized in this region (Fig. 9c). The titration was not extended beyond R = 1.0 due to precipitation of the ligand.

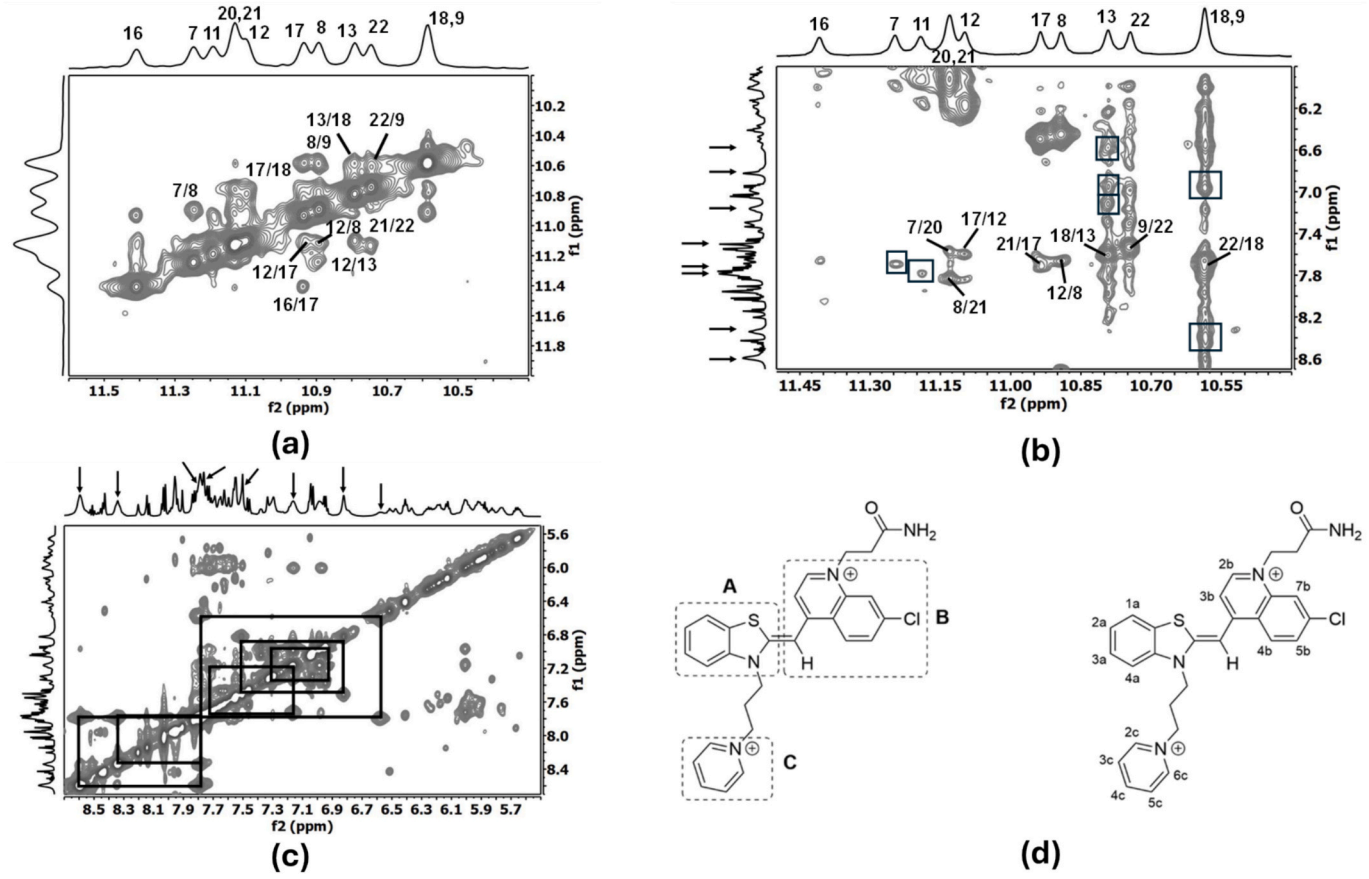


**Fig. 8.** Expanded 2D NOESY spectrum of the Pu22T14T23:R9 complex, showing (a) the inter-residue connectivities NH-NH within the tetrad planes; (b) the NOE interactions of the aromatic protons of R9 with imino protons (in the squares) and inter-residue cross peaks between aromatic and imino protons in the tetrads; (c) R9 aromatic protons (arrows); (d) R9 structure with proton and ring coding.

Chemical shift perturbations observed in the NMR titration experiments with R9 and QDJ1 are consistent—similarly to what was observed for dye 3b —with ligand association at the G4–duplex junction region (Fig. 10). However, the pronounced line broadening indicates an intermediate exchange regime between the free and bound states, which does not allow a detailed interpretation of the spectra and prevents unambiguous resonance assignment.

### 3.6.3. *Molecular modeling and docking studies*

Molecular modeling studies provided further insights into the binding modes of both dyes (Figs. 11 and 12). In both cases, the ligands are effectively anchored to the G4 structures via the positively charged nitrogen atoms. Additionally, in the case of R9, the flexible side chain bearing the charged pyridinium group enhances the ligand's binding to the anionic grooves of the oligonucleotides.

*3.6.3.1. Pu22T14T23:3b complex.* Structural analysis of the Pu22T14T23 complex with 3b reveals that the ligand binds to the external G-tetrads through π-π stacking interactions involving the ring systems A and B. Specifically, at the 5′-end, stacking occurs with G7, G11, and G16, while at the 3′-end, interactions involve G13 and G18. In addition, ionic interactions are predicted between the charged nitrogen on ring system B and phosphate groups from T23, G11, T14, and G16. The model also suggests a degree of freedom of 3b within the binding sites (Fig. 11a and b; Fig. S5).

*3.6.3.2. Pu22T14T23:R9 complex.* Detailed structural analysis of the Pu22T14T23:R9 complex highlights the presence of π-π stacking interactions at two distinct binding sites. At the 5′-end, R9 interacts with G11 via ring system B, while the benzene ring of system A stacks on G7. Additionally, the primary amide group of side chain forms a hydrogen bond with the G16 residue. This binding mode is influenced by the electrostatic features of R9, which contains two positively charged centers. The double cationic nature of the ligand enhances G4 recognition and binding, notably through an additional electrostatic interaction between the charged pyridinium ring C and G11. At the 3′-end, π-π stacking involves G13 and G18, while the amide group engages in a hydrogen bond with G17, and the positively charged nitrogen on ring system B contributes to electrostatic stabilization with G18 (Fig. 11c and d; Fig. S6).

*3.6.3.3. QDJ1:3b complex.* The docking studies suggest that dye 3b can adopt two alternative orientations within the QDJ1 binding site, giving rise to complexes 1 and 2. In pose 1 (Fig. 12a), both ring systems A and B partially stack on exposed bases at the G-tetrad–duplex junction, interacting with C20, G1, G6 and C7. Ring system A is oriented toward the groove, extending in the direction of the hairpin loop, and establishes contacts with C7 (Fig. S7). In pose 2 (Fig. 12b), ring system A stacks on the guanine tetrad, while ring system B is accommodated within the groove of the oligonucleotide.

*3.6.3.4. QDJ1:R9 complex.* The binding mode of R9 within the QDJ1 structure is shown in Fig. 12c and d. Both ring systems A and B are intercalated at the quadruplex-duplex junction. The charged pyridinium ring C extends away from the junction, adopting two possible orientations: one directed toward G5 and G6 (Fig. 12c and S8), the other toward C20 and G19 (Fig. 12d and S8), where it forms electrostatic interactions with the phosphate backbone. The positively charged nitrogen of ring

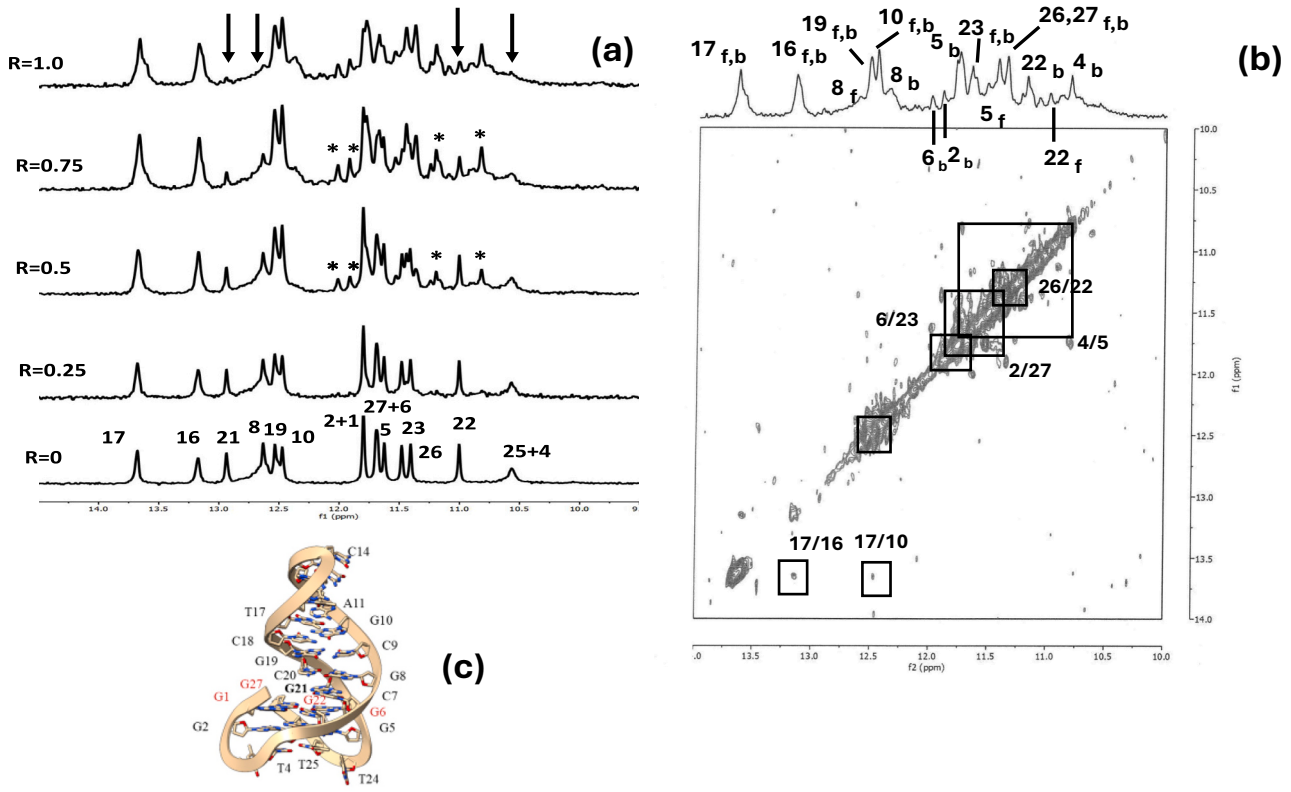


**Fig. 9.** (a) Imino proton region of the 1D NMR titration spectra of QDJ1 with 3b at 5 °C in $H_2O/D_2O$ (9:1), 10 mM $KH_2PO_4$, 50 mM KCl, pH 7.0, at different R = [3b]:[DNA] ratios. The arrows show signals that disappear, and the asterisks show new signals in slow chemical exchange; (b) Imino proton region of NOESY spectrum at 5 °C in $H_2O/D_2O$ (9:1), 10 mM $KH_2PO_4$, 50 mM KCl, pH 7.0, at R = [3b]:[DNA] =1.0; (c) a schematic representation of QDJ1, the perturbations detected were consistent with selective binding of 3b to the quadruplex-duplex junction region.

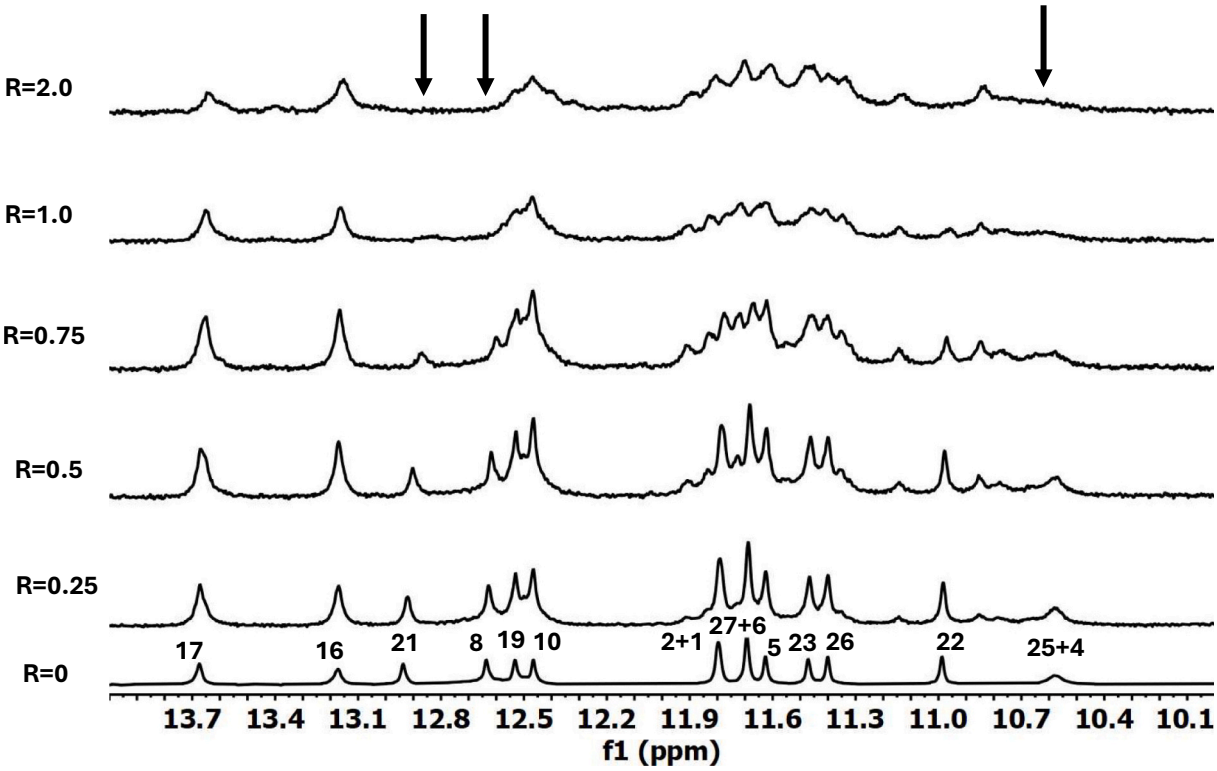


**Fig. 10.** Imino proton region of the 1D NMR titration spectra of QDJ1 with R9 at 5 °C in $H_2O/D_2O$ (9:1), 10 mM $KH_2PO_4$, 50 mM KCl, pH 7.0, at different R = [R9]:[DNA] ratios. The arrows show signals that disappear. These findings were consistent with s binding of R9 to the quadruplex-duplex junction region.

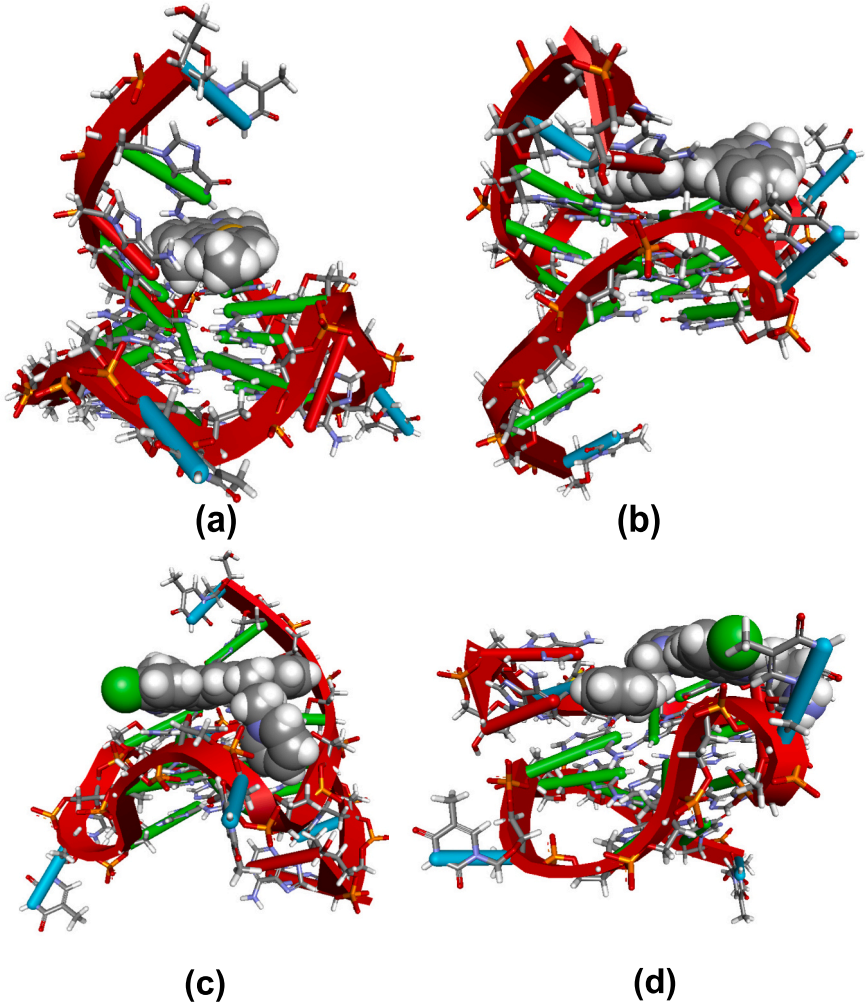


**Fig. 11.** Molecular models of 3b and R9 with Pu22T14T23. Side views of the best docked conformations for 3b at the 5′-end (a) and at the 3′-end (b) binding site. Side views of the best docked conformations for R9 at the 5′-end (c) and at the 3′-end (d) binding site. Nucleic acid is represented as an arrow along the backbone. Thymine bases are represented in blue, adenines in red and guanines in green. Ligands are in CPK. Molecular interactions are reported in detail in Figs. S5 and S6. (For interpretation of the references to color in this figure legend, the reader is referred to the web version of this article.)

system B engages in ionic interactions with G19, G21, and G27. Furthermore, the amide group on side chain forms hydrogen bonds with G1 and G27.

### *3.7. Selective fluorescence properties of dyes in presence of DNA structures*

Following the study of the dyes and DNA, their fluorescence properties were examined. None of the dyes exhibited intrinsic fluorescence due to several nonradiative decay mechanisms, but they can become highly fluorescent upon binding structured biomolecules like DNA. For dyes R9 and 3b, the addition of DNA sequences able to form secondary structures clearly produced the appearance of fluorescence in the green region of the visible spectrum. For example, the excitation-emission maps (EEM) of mixtures of Pu22T14T23 and QDJ1 with dyes R9 and 3b are shown in Fig. 13a and Fig. 13b, respectively. The dye R9 showed green fluorescence with excitation at 520 and emission at 540 nm, approximately, with a small spectral shift depending on the DNA structure. On the other hand, the fluorescence of dye 3b was maximal at excitation 520 and emission 535 nm.

Fig. 13c shows the normalized fluorescent intensity of all DNA:dye complexes, expressed relative to the fluorescent intensity of the DNA structure that produces the strongest signal for each dye. It was observed that R9 showed more fluorescence in the presence of structures that incorporate a double-helix segment (h28 and QDJ1), whereas dye 3b was more selective toward parallel G4 structures, such as that formed by Pu22T14T23. Surprisingly, only residual fluorescence appeared in the presence of TBA. An explanation is the sterically hindered shape of TBA with nucleobases oriented toward the interior (Fig. 1e). Another explanation could be the flexible structure of TBA, allowing more torsional freedom of dye molecules on the oligomer surface.

## 4. Conclusions

Recently, the interaction between the cyanine dyes R9 and 3b, which differ in electric charge and polarity, with single stranded A-RNA and double stranded B-DNA has been investigated [18,22]. Their potential as nucleic acid probes was explored using molecular absorption and fluorescence spectroscopies. In the present study, we have extended that work by examining the interaction of these two dyes with various G4 structures, with particular emphasis on the thermodynamic and structural aspects. As previously noted, the potential for tuning G4 stability through interaction with selective ligands is a topic of considerable interest in both biology and nanotechnology. In this context, G4-duplex junctions, such as those formed by the QDJ1 sequence, represent promising targets for selective DNA-ligand interaction [10,47].

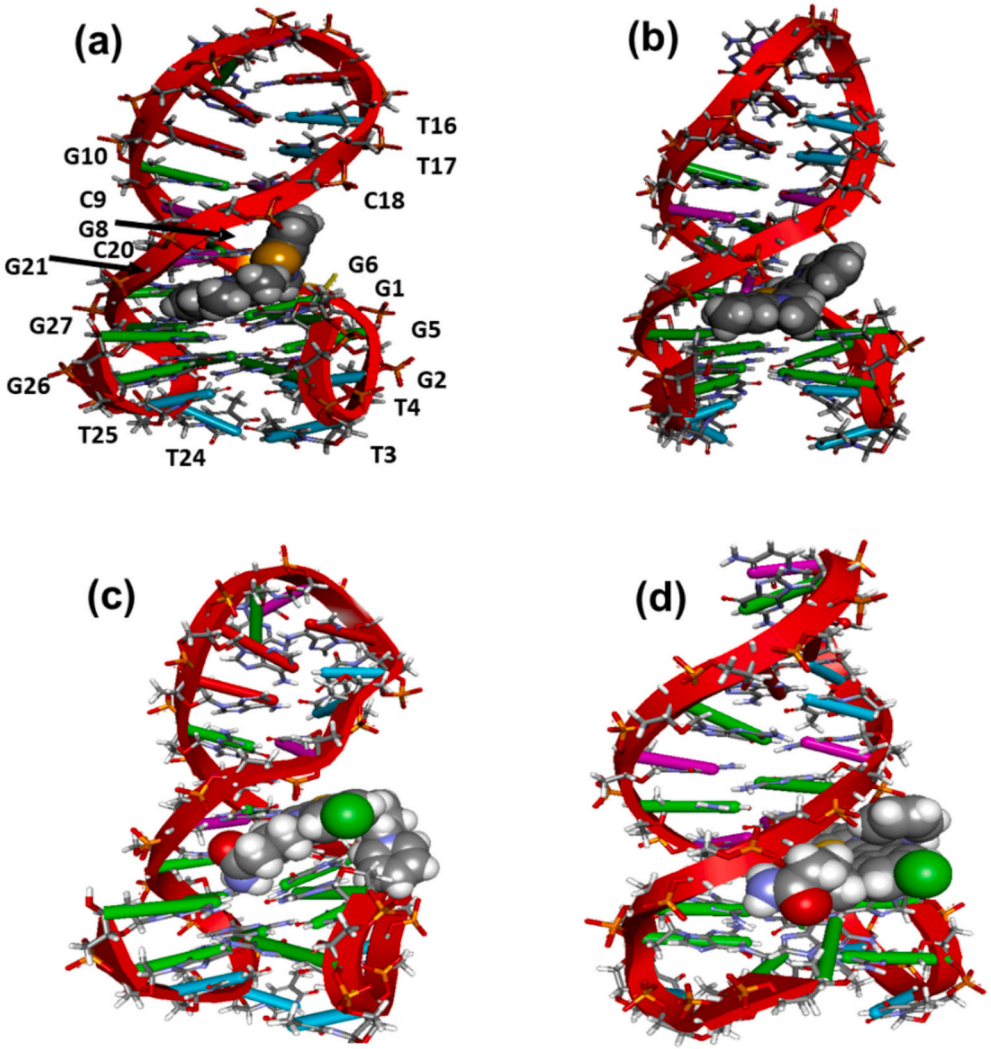


**Fig. 12.** Docking poses of the complex QDJ1:3b obtained by Molecular Docking. (a) Side view of complex A. (b) Side view of complex B. Docking poses of the complex QDJ1:R9 obtained by Molecular Docking. (c) Side view of complex A. (d) Side view of complex B. Nucleic acid is represented as an arrow along the backbone. The nucleotides are represented as follows: Adenine in red, Guanine in green, Thymine in blue and Cytosine in violet. Ligand is in CPK colored by atoms. Molecular interactions are reported in detail in Figs. S7 and S8. (For interpretation of the references to color in this figure legend, the reader is referred to the web version of this article.)

The results of the present work have revealed distinct behaviors of the considered dyes in aqueous solution, which influence their interactions with the DNA structures studied. The more polar dye (R9) exhibits a simpler binding mechanism, whereas the less polar dye (3b) tends to aggregate on aqueous media and on the surface of G4 structures. These differences seem to correlate with their distinct fluorescence properties. While the dye R9 shows an intense fluorescence in the presence of duplex regions (such as those present in h28 or QDJ1 sequences), the dye 3b shows an increase in its signal in presence of the parallel G4 formed by Pu22T14T23 sequence. The dye 3b, however, does not show a clear enhancement of fluorescence in the presence of the TBA antiparallel G4 structure. The ICD signal observed for dye 3b in presence of Pu22T14T23 and TBA suggests that the dye binds in a chiral environment. However, only the parallel G4 provides a flat, rigid platform that allows for both π-stacking and rotational restriction, hence the strong fluorescence observed in presence of Pu22T14T23. In contrast, the antiparallel G4 (TBA) supports chiral dye orientation but not enough restriction of motion likely due to the loop orientation, which affects the available surface at the chromophore binding site [15,48]. This could be the reason why fluorescence enhancement is poor, despite ICD being present. For the G4–duplex junction, NMR analysis and molecular docking confirm that the interaction of dyes occurs specifically at the junction between the two structures. CD dichroism and molecular docking pointed to some structural changes of DNA in the presence of the dyes; an interaction that stabilizes strongly the structure, according to the melting experiments.

In summary, due to the described structural features and the properties influenced by them, it can be concluded that dye 3b could be used as a molecular sensor for the detection and visualization of parallel G4 structures such as that formed by Pu22T14T23, whereas dye R9 would be more convenient for the detection of structures including duplex moieties. This thermodynamic and structural description will be followed by a study of the kinetics of the interaction of both dyes with the considered DNA structures.

## CRediT authorship contribution statement

**Aleksey Vasilev:** Investigation, Formal analysis, Conceptualization. **Diana Cheshmedzhieva:** Investigation, Formal analysis, Conceptualization. **Hamzah Ahmed:** Writing – review & editing, Investigation, Formal analysis. **Ona Raset:** Investigation, Formal analysis. **Gigliola Borgonovo:** Investigation, Formal analysis. **Stefania Mazzini:** Writing

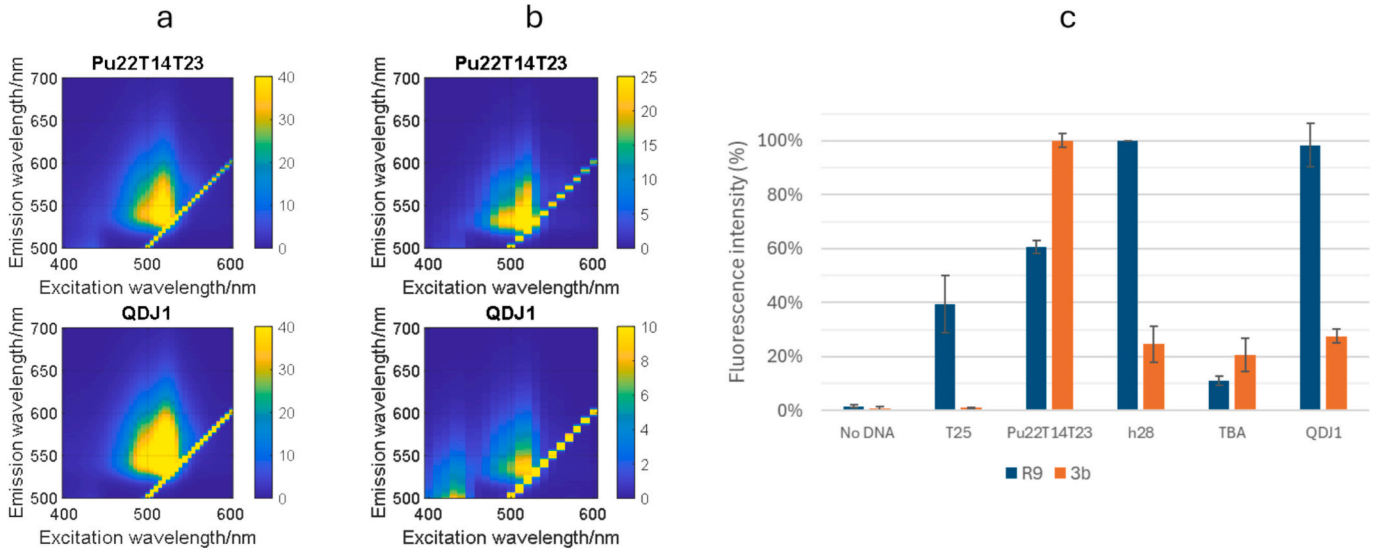


**Fig. 13.** Excitation-emission fluorescence maps measured for mixtures involving Pu22T14T23 and QDJ1 sequences and R9 (a), and 3b (b), and normalized fluorescence intensities measured for all DNA:dye mixtures (c). Dye and DNA concentrations were 0.7 and 2 micromolar, respectively. Measurements conducted in 20 mM phosphate buffer pH 7.4, and 50 mM KCl. The temperature was 15 °C. Voltage was set to 600 V in all cases.

– review & editing, Investigation, Formal analysis. **Roberto Artali:** Writing – review & editing, Investigation, Formal analysis. **Marco Zuccolo:** Investigation, Formal analysis. **Raimundo Gargallo:** Writing – review & editing, Supervision, Software, Project administration, Methodology, Conceptualization.

## Declaration of competing interest

The authors declare that they have no known competing financial interests or personal relationships that could have appeared to influence the work reported in this paper.

## Acknowledgments

Claudia Xicota and Junjie Zhou (University of Barcelona) are thanked for their help in conducting some of the experiments. This study was supported by grant PID2023-146465NB-I00 funded by MICIU/AEI/10.13039/501100011033 and "ERDF A way of making Europe". The NMR spectra at 600 MHz were acquired thanks to the facilities of Unitech COSPECT ("Linea 2", Milano, Italy). Aleksey Vasilev and Diana Cheshmedzhieva kindly acknowledge the funding by the European Union-NextGenerationEU, through the National Recovery and Resilience Plan of the Republic of Bulgaria, project SUMMIT BG-RRP-2.004-0008 C01 (70-123-216/12.02.2024).

## Appendix A. Supplementary data

Supplementary data to this article can be found online at https://doi.org/10.1016/j.ijbiomac.2025.146636.

## Data availability

Data will be made available on request.

## References

[1] F. Romano, A. Di Porzio, N. Iaccarino, G. Riccardi, R. Di Lorenzo, S. Laneri, B. Pagano, J. Amato, A. Randazzo, G-quadruplexes in cancer-related gene promoters: from identification to therapeutic targeting, Expert Opin. Ther. Pat. 33 (2023) 745–773, https://doi.org/10.1080/13543776.2023.2271168.
[2] S. Neidle, Quadruplex nucleic acids as novel therapeutic targets, J. Med. Chem. 59 (2016) 5987–6011, https://doi.org/10.1021/acs.jmedchem.5b01835.
[3] C. Roxo, A. Pasternak, Switching off cancer – an overview of G-quadruplex and i-motif functional role in oncogene expression, Bioorg. Med. Chem. Lett. 116 (2025) 130038, https://doi.org/10.1016/j.bmcl.2024.130038.
[4] J. Carvalho, J.-L. Mergny, G.F. Salgado, J.A. Queiroz, C. Cruz, G-quadruplex, friend or foe: the role of the G-quartet in anticancer strategies, Trends Mol. Med. 26 (2020) 848–861, https://doi.org/10.1016/j.molmed.2020.05.002.
[5] J.E. Reed, A.A. Arnal, S. Neidle, R. Vilar, Stabilization of G-quadruplex DNA and inhibition of telomerase activity by square-planar nickel(II) complexes, J. Am. Chem. Soc. 128 (2006) 5992–5993, https://doi.org/10.1021/ja058509n.
[6] J. Carvalho, A. Paiva, M.P. Cabral Campello, A. Paulo, J.-L. Mergny, G.F. Salgado, J.A. Queiroz, C. Cruz, Aptamer-based targeted delivery of a G-quadruplex ligand in cervical Cancer cells, Sci. Rep. 9 (2019) 7945, https://doi.org/10.1038/s41598-019-44388-9.
[7] M. Gunaratnam, S. Swank, S.M. Haider, K. Galesa, A.P. Reszka, M. Beltran, F. Cuenca, J.A. Fletcher, S. Neidle, Targeting human gastrointestinal stromal tumor cells with a quadruplex-binding small molecule, J. Med. Chem. 52 (2009) 3774–3783, https://doi.org/10.1021/jm900424a.
[8] A.K. Todd, S. Neidle, The relationship of potential G-quadruplex sequences in cis-upstream regions of the human genome to SP1-binding elements, Nucleic Acids Res. 36 (2008) 2700–2704, https://doi.org/10.1093/nar/gkn078.
[9] P.A. Rachwal, T. Brown, K.R. Fox, Effect of G-tract length on the topology and stability of intramolecular DNA Quadruplexes, Biochemistry 46 (2007) 3036–3044, https://doi.org/10.1021/bi062118j.
[10] L. Díaz-Casado, I. Serrano-Chacón, L. Montalvillo-Jiménez, F. Corzana, A. Bastida, A.G. Santana, C. González, J.L. Asensio, De Novo Design of Selective Quadruplex–Duplex Junction Ligands and Structural Characterisation of Their Binding Mode: Targeting the G4 Hot-Spot, Chem. Eur. J. 27 (2021) 6204–6212, https://doi.org/10.1002/chem.202005026.
[11] K.W. Lim, A.T. Phan, Structural Basis of DNA Quadruplex–Duplex Junction Formation, Angew. Chem. Int. Ed. 52 (2013) 8566–8569, https://doi.org/10.1002/anie.201302995.
[12] S. Mazzini, G. Borgonovo, S. Princiotto, R. Artali, L. Musso, A. Aviñó, R. Eritja, R. Gargallo, S. Dallavalle, Quadruplex-duplex junction in LTR-III: a molecular insight into the complexes with BMH-21, namitecan and doxorubicin, PLoS One 19 (2024) e0306239, https://doi.org/10.1371/journal.pone.0306239.
[13] K.W. Lim, P. Jenjaroenpun, Z.J. Low, Z.J. Khong, Y.S. Ng, V.A. Kuznetsov, A. T. Phan, Duplex stem-loop-containing quadruplex motifs in the human genome: a combined genomic and structural study, Nucleic Acids Res. 43 (2015) 5630–5646, https://doi.org/10.1093/nar/gkv355.
[14] J. Figueiredo, J.-L. Mergny, C. Cruz, G-quadruplex ligands in cancer therapy: Progress, challenges, and clinical perspectives, Life Sci. 340 (2024) 122481, https://doi.org/10.1016/j.lfs.2024.122481.
[15] A. Arora, S. Maiti, Effect of loop orientation on Quadruplex−TMPyP4 interaction, J. Phys. Chem. B 112 (2008) 8151–8159, https://doi.org/10.1021/jp711608y.
[16] E.W. White, F. Tanious, M.A. Ismail, A.P. Reszka, S. Neidle, D.W. Boykin, W. D. Wilson, Structure-specific recognition of quadruplex DNA by organic cations: influence of shape, substituents and charge, Biophys. Chem. 126 (2007) 140–153, https://doi.org/10.1016/j.bpc.2006.06.006.
[17] N. Ishkitiev, M. Miteva, M. Micheva, T. Stoyanova, V.V. Lozanova, V.S. Lozanov, Z. Mihaylova, D.V. Cheshmedzhieva, M. Kandinska, M. Rangelov, N. Todorova, S. Ilieva, S. Baluschev, R. Gargallo, B. Calenic, I. Constantinescu, K. Landfester, A. A. Vasilev, Aggregation induced nucleic acids recognition by homodimeric asymmetric monomethyne cyanine fluorochromes in mesenchymal stem cells, Int.

J. Biol. Macromol. 250 (2023) 126094, https://doi.org/10.1016/j.ijbiomac.2023.126094.
[18] N. Ishkitiev, M. Micheva, M. Miteva, S. Gaydarova, C. Tzachev, V. Lozanova, V. Lozanov, D. Cheshmedzhieva, M. Kandinska, S. Ilieva, R. Gargallo, S. Baluschev, S. Stoynov, T. Dyankova-Danovska, M. Nedelcheva-Veleva, K. Landfester, Z. Mihaylova, A. Vasilev, Nanoconfined chlorine-substituted Monomethine cyanine dye with a Propionamide function based on the Thiazole Orange scaffold—use of a Fluorogenic probe for cell staining and nucleic acid visualization, Molecules 29 (2024) 6038, https://doi.org/10.3390/molecules29246038.
[19] J. Robinson, S.G. Stenspil, K. Maleckaite, M. Bartlett, M. Di Antonio, R. Vilar, M. K. Kuimova, Cellular Visualization of G-Quadruplex RNA via Fluorescence-Lifetime Imaging Microscopy, J. Am. Chem. Soc. 146 (2024) 1009–1018, https://doi.org/10.1021/jacs.3c11908.
[20] L. Zhang, X. Liu, S. Lu, J. Liu, S. Zhong, Y. Wei, T. Bing, N. Zhang, D. Shangguan, Thiazole orange styryl derivatives as fluorescent probes for G-quadruplex DNA, ACS Appl. Bio Mater. 3 (2020) 2643–2650, https://doi.org/10.1021/acsabm.9b01243.
[21] R. Nanjunda, E. Owens, L. Mickelson, T. Dost, E. Stroeva, H. Huynh, M. Germann, M. Henary, W. Wilson, Selective G-Quadruplex DNA recognition by a new class of designed Cyanines, Molecules 18 (2013) 13588–13607, https://doi.org/10.3390/molecules181113588.
[22] S. Ilieva, N. Petkov, R. Gargallo, C. Novakov, M. Rangelov, N. Todorova, A. Vasilev, D. Cheshmedzhieva, Bioaggregachromism of asymmetric Monomethine cyanine dyes as noncovalent binders for nucleic acids, Biosensors (Basel) 15 (2025) 187, https://doi.org/10.3390/bios15030187.
[23] C. Ji, Y. Song, Z. Fan, L. Liu, Y. Sun, R. Yang, C. Ma, Y. Cai, D. Miao, C. Huang, R. Xiong, Physical Intracellular Delivery Based on Microfluidic Technology, Small n/a (2025) 2504048, https://doi.org/10.1002/smll.202504048.
[24] A. Ambrus, D. Chen, J. Dai, R.A. Jones, D. Yang, Solution structure of the biologically relevant G-quadruplex element in the human c-MYC promoter. Implications for G-quadruplex stabilization, Biochemistry 44 (2005) 2048–2058, https://doi.org/10.1021/bi048242p.
[25] P. Schultze, R.F. Macaya, J. Feigon, Three-dimensional solution structure of the thrombin-binding DNA aptamer d(GGTTGGTGTGGTTGG), J. Mol. Biol. 235 (1994) 1532–1547, https://doi.org/10.1006/jmbi.1994.1105.
[26] L. Musso, S. Mazzini, A. Rossini, L. Castagnoli, L. Scaglioni, R. Artali, M. Di Nicola, F. Zunino, S. Dallavalle, C-MYC G-quadruplex binding by the RNA polymerase I inhibitor BMH-21 and analogues revealed by a combined NMR and biochemical approach, Biochim. Biophys. Acta Gen. Subj. 1862 (2018) 615–629, https://doi.org/10.1016/j.bbagen.2017.12.002.
[27] E. Krieger, G. Vriend, New ways to boost molecular dynamics simulations, J. Comput. Chem. 36 (2015) 996–1007, https://doi.org/10.1002/jcc.23899.
[28] O. Trott, A.J. Olson, AutoDock Vina: improving the speed and accuracy of docking with a new scoring function, efficient optimization, and multithreading, J. Comput. Chem. 31 (2010) 455–461, https://doi.org/10.1002/jcc.21334.
[29] R. Galindo-Murillo, J.C. Robertson, M. Zgarbová, J. Šponer, M. Otyepka, P. Jurečka, T.E. Cheatham, Assessing the current state of Amber force field modifications for DNA, J. Chem. Theory Comput. 12 (2016) 4114–4127, https://doi.org/10.1021/acs.jctc.6b00186.
[30] B.I.O.V.I.A. Dassault Systèmes, BIOVIA Discovery Studio Visualize, 2019.
[31] J.-L. Mergny, L. Lacroix, Analysis of thermal melting curves, Oligonucleotides 13 (2003) 515–537, https://doi.org/10.1089/154545703322860825.
[32] K.J. Breslauer, [10] extracting thermodynamic data from equilibrium melting curves for oligonucleotide order-disorder transitions, in: Methods Enzymol, Academic Press, 1995, pp. 221–242, https://doi.org/10.1016/0076-6879(95)59046-3.
[33] L. Bchara, R. Eritja, R. Gargallo, F. Benavente, Rapid and highly efficient separation of i-motif DNA species by CE-UV and multivariate curve resolution, Anal. Chem. 95 (2023) 15189–15198, https://doi.org/10.1021/acs.analchem.3c01730.
[34] S. Benabou, C. Ruckebusch, M. Sliwa, A. Aviñó, R. Eritja, R. Gargallo, A. De Juan, Study of conformational transitions of i-motif DNA using time-resolved fluorescence and multivariate analysis methods, Nucleic Acids Res. 47 (2019), https://doi.org/10.1093/nar/gkz522.
[35] S. Benabou, C. Ruckebusch, M. Sliwa, A. Aviñó, R. Eritja, R. Gargallo, A. de Juan, Study of light-induced formation of photodimers in the i-motif nucleic acid structure by rapid-scan FTIR difference spectroscopy and hybrid hard- and soft-modelling, Phys. Chem. Chem. Phys. 20 (2018) 19635–19646, https://doi.org/10.1039/C8CP00850G.
[36] C. Poyato, J. Pacheco, A. Domínguez, R. Eritja, A. Aviñó, R. Gargallo, Assessment of methodologies based on the formation of antiparallel triplex DNA structures and fluorescent silver nanoclusters for the detection of pyrimidine-rich sequences, Spectrochim. Acta A Mol. Biomol. Spectrosc. 329 (2025) 125567, https://doi.org/10.1016/j.saa.2024.125567.
[37] R. Gargallo, R. Tauler, A. Izquierdo-Ridorsa, Application of a multivariate curve resolution procedure to the analysis of second-order melting data of synthetic and natural polynucleotides, Anal. Chem. 69 (1997) 1785–1792, https://doi.org/10.1021/ac960809n.
[38] N.C. Maiti, S. Mazumdar, N. Periasamy, J- and H-aggregates of porphyrin−surfactant complexes: time-resolved fluorescence and other spectroscopic studies, J. Phys. Chem. B 102 (1998) 1528–1538, https://doi.org/10.1021/jp9723372.
[39] T.Y. Ogul'chansky, M.Y. Losytskyy, V.B. Kovalska, V.M. Yashchuk, S.M. Yarmoluk, Interactions of cyanine dyes with nucleic acids. XXIV. Aggregation of monomethine cyanine dyes in presence of DNA and its manifestation in absorption and fluorescence spectra, Spectrochim. Acta A Mol. Biomol. Spectrosc. 57 (2001) 1525–1532, https://doi.org/10.1016/S1386-1425(01)00437-1.
[40] W. West, S. Pearce, The dimeric state of cyanine dyes, J. Phys. Chem. 69 (1965) 1894–1903, https://doi.org/10.1021/j100890a019.
[41] S. Berndl, S.D. Dimitrov, F. Menacher, T. Fiebig, H. Wagenknecht, Thiazole Orange dimers in DNA: Fluorescent Base substitutions with hybridization readout, Chem. Eur. J. 22 (2016) 2386–2395, https://doi.org/10.1002/chem.201503849.
[42] M.J. Frisch, G.W. Trucks, H.B. Schlegel, G.E. Scuseria, M.A. Robb, J.R. Cheeseman, G. Scalmani, V. Barone, G.A. Petersson, H. Nakatsuji, X. Li, M. Caricato, A. V. Marenich, J. Bloino, B.G. Janesko, R. Gomperts, B. Mennucci, H.P. Hratchian, J. V. Ortiz, A.F. Izmaylov, J.L. Sonnenberg, D. Williams-Young, F. Ding, F. Lipparini, F. Egidi, J. Goings, B. Peng, A. Petrone, T. Henderson, D. Ranasinghe, V. G. Zakrzewski, J. Gao, N. Rega, G. Zheng, W. Liang, M. Hada, M. Ehara, K. Toyota, R. Fukuda, J. Hasegawa, M. Ishida, T. Nakajima, Y. Honda, O. Kitao, H. Nakai, T. Vreven, K. Throssell, J.A. Montgomery Jr., J.E. Peralta, F. Ogliaro, M. J. Bearpark, J.J. Heyd, E.N. Brothers, K.N. Kudin, V.N. Staroverov, T.A. Keith, R. Kobayashi, J. Normand, K. Raghavachari, A.P. Rendell, J.C. Burant, S.S. Iyengar, J. Tomasi, M. Cossi, J.M. Millam, M. Klene, C. Adamo, R. Cammi, J.W. Ochterski, R.L. Martin, K. Morokuma, O. Farkas, J.B. Foresman, D.J. Fox, Gaussian 16, Revision 16.A.03, 2016.
[43] S. Paramasivan, I. Rujan, P.H. Bolton, Circular dichroism of quadruplex DNAs: applications to structure, cation effects and ligand binding, Methods 43 (2007) 324–331, https://doi.org/10.1016/j.ymeth.2007.02.009.
[44] S. Masiero, R. Trotta, S. Pieraccini, S. De Tito, R. Perone, A. Randazzo, G.P. Spada, A non-empirical chromophoric interpretation of CD spectra of DNA G-quadruplex structures, Org. Biomol. Chem. 8 (2010) 2683, https://doi.org/10.1039/c003428b.
[45] K.M. Sovenyhazy, J.A. Bordelon, J.T. Petty, Spectroscopic studies of the multiple binding modes of a trimethine-bridged cyanine dye with DNA, Nucleic Acids Res. 31 (2003) 2561–2569, https://doi.org/10.1093/nar/gkg363.
[46] N.C. Garbett, P.A. Ragazzon, J.B. Chaires, Circular dichroism to determine binding mode and affinity of ligand-DNA interactions, Nat. Protoc. 2 (2007) 3166–3172, https://doi.org/10.1038/nprot.2007.475.
[47] L. Scott, T.V. Chalikian, Stabilization of G-Quadruplex-duplex hybrid structures induced by minor groove-binding drugs, Life 12 (2022) 597, https://doi.org/10.3390/life12040597.
[48] S.M. Haider, I. Autiero, S. Neidle, Surface area accessibility and the preferred topology of telomeric DNA quadruplex–ligand complexes, Biochimie 93 (2011) 1275–1279, https://doi.org/10.1016/j.biochi.2011.05.014.